Yttrium zoning in garnet: Coupling of major and accessory phases during metamorphic reactions

Joseph M. Pyle[1] and Frank S. Spear[2]

Department of Earth and Environmental Sciences, Rensselaer Polytechnic Institute, Troy, NY 12180, USA
[1]<pylej@rpi.edu> [2]<spearf@rpi.edu>
(Received:July 10, 1999; Published: December 14, 1999)

Abstract

The concentration of yttrium in pelitic garnets as a function of metamorphic grade has been examined in relation to the distribution of xenotime (YPO_4) in samples from New England and British Columbia. Samples with xenotime present only as inclusions in garnet generally possess high-Y cores and concentrations that drop off discontinuously along zoning shoulders of variable width to low-Y outboard regions. Samples with matrix xenotime are restricted to the garnet zone; Y concentration of these garnets generally decreases smoothly from core to rim. Xenotime may also be present in reaction zones around garnet. In xenotime-bearing samples, $[Y]_{Grt}$ is strongly temperature-dependent and ranges from ~5000 ppm in the garnet zone to ~150 ppm in the sillimanite zone. Measured yttrium zoning profiles in xenotime-absent samples are reproduced with both Rayleigh fractionation and diffusion models, but P-T histories of the samples examined favor the Rayleigh model, with garnet volume, bulk-rock yttrium, and mode of (Y,HREE) accessory phases controlling the profile shape. High-yttrium annuli in staurolite-zone samples may form by garnet overgrowth of proximal matrix enriched in yttrium due to garnet consumption during discontinuous staurolite-forming reactions. An increase in $[Y]_{Grt}$ and $[HREE]_{Grt}$ in garnet from anatectic samples is related to dissolution of phosphates in vapor-absent, peraluminous melt, with partitioning of highly compatible Y and HREE into garnet grown during anatexis; textural analysis reveals that phosphates are absent from regions of garnet grown in equilibrium with melt. A main result of this study is identification of an intimate coupling between major pelite phases and accessory phases during reaction progress. This coupling is of great advantage in that it may be used to: (1) calibrate sensitive geothermometers and geobarometers, (2) identify particular regions of garnet grown in different garnet-producing reactions over a range of grades, and (3) reveal portions of pelite reaction history invisible to major elements.

Keywords: garnet, pelite, xenotime, yttrium, trace element, zoning.

Introduction

The development of techniques for mapping in-situ distributions of elements in metamorphic garnet has become a nearly indispensable tool for recent studies involving computation of P-T paths for metamorphic rocks (Spear and Kohn, 1996; Kohn et al., 1997). The above works and Lanzirotti (1995) also highlight the notable differences between major- and trace-element distributions in garnet. The hypotheses drawn from these works are: 1) trace elements are extremely sensitive to changes in accessory mineral assemblage and/or fluid composition, and; 2) many trace-element diffusivities in garnet must be very much slower than diffusivities for major divalent (Mg, Fe, Mn) cations in garnet, but possibly on the same order as the diffusivity of Ca in garnet.

The element yttrium is a notable trace constituent particularly compatible with garnet. Jaffe (1951) demonstrated that a correlation exists between manganese content and yttrium content in garnet, and measured the yttrium content of several pegmatitic and granitic garnets (maximum 2.64 wt % Y_2O_3). He also predicted that a pure yttrium garnet ($Y_3Al_2Al_3O_{12}$, or YAG) would require aluminum in both octahedral and tetrahedral coordination. Such a compound with the garnet structure was synthesized shortly thereafter by Yoder and Keith (1951). Pelitic garnets have also been shown to contain moderate amounts of Y; garnets from the Straits schist, Connecticut (Lanzirotti, 1995) contain up to 5000 ppm Y, whereas other major pelite phases in this formation contain 2-5 ppm Y (quartz) and 200-300 ppm Y (biotite and muscovite) (Lanzirotti, 1995). These values indicate that yttrium partitioning among major pelitic minerals will strongly (100-1000x) favor garnet, and that the mode of major pelite phases besides garnet will have little effect on yttrium fractionation. Yang et al. (1999) examined biotite-garnet trace-element partitioning in lower-greenschist to upper-amphibolite facies pelites and quartzofeldspathic gneisses from western Labrador. In analyses from 27 samples, maximum Y content of biotite is 2 ppm, with yttrium below detection limits in biotites from 9 of the 27 samples. Garnet in the samples contains from 1 to 706 ppm Y, with garnets in all but four of the samples having $[Y]_{Grt} > 50$ ppm.

However, several studies indicate that the majority of the trace-element budget of a given sample resides within accessory phases. For example, Reid (1990) estimated that up to 60% of the REE mass budget of migmatitic granulites may be contained in accessory phases. Wark and Miller (1993) estimated that ≥ 95 % of bulk-rock Y, REE, Zr, Hf, and P found in samples from the Sweetwater Wash pluton resides in accessory phases. Therefore, the presence, absence, growth, and consumption of accessory phases enriched in yttrium (and HREE as well) plays an important role in controlling the distribution of Y throughout a rock. An accessory phase likely to exert a significant control on Y distribution is the phosphate xenotime, $(Y,HREE)PO_4$. To a first approximation, pelitic xenotime can be considered a Y-saturating phase, and if present, buffers the activity of YPO_4 (a_{YPO4}) in the rock. If garnet is growing at constant a_{YPO4}, the distribution of yttrium is controlled by the P-T behavior of the equilibrium describing mass action between Y in garnet and Y in xenotime. Pyle and Spear (1999a) have demonstrated that there is a very strong temperature control on $[Y]_{Grt}$ in xenotime-bearing assemblages. Their empirical calibration of the xenotime-YAG geothermometer has a temperature resolution of approximately ± 3 °C at low grades.

Accessory phases such as monazite, epidote, zircon, apatite, and titanite, while not saturating yttrium, can incorporate significant amounts of yttrium (e.g. Görz and White, 1970; Exley, 1980; Deer et al., 1992; Franz et al., 1996; Wopenka et al., 1996; Heinrich et al., 1997; Finger et al., 1998), and will have a pronounced effect on yttrium fractionation if xenotime is absent. Yttrium fractionation in xenotime-absent rocks will be controlled, to a large extent, by the above minerals if they are present in sufficient abundance.

Because accessory phases exert a first-order control on the trace-element budget in pelites, knowledge of their distribution is critical to understanding trace element distribution in garnet. To this end, we present observations on the distribution of xenotime in pelitic schists as a function of metamorphic grade and major mineral assemblage, and relate these observations to the concentration of yttrium in coexisting garnet. One of the primary conclusions of this study is that accessory phases appear to participate in major-phase pelite reactions at all grades.

Regional setting and sample selection

Pelites with well-characterized P-T histories from three different areas were chosen for study. The majority of samples examined come from the Ordovician and Silurian metasediments of the Bronson Hill Anticlinorium and Merrimack Synclinorium, west-central New Hampshire. (Thompson et al., 1968; Robinson et al., 1991; Spear, 1992). The region has undergone at least three periods of deformation: an early nappe-and-thrust sequence, followed by gneiss dome formation with related folding about north-south fold axes, and a later period of open folding with east-west trending fold axes (Chamberlain, 1986). The dominant fabric in these samples is designated S_2, which varies from a spaced cleavage to a pervasive foliation. S_2 was correlated by Spear et al. (1995) with the regional nappe formation. S_0 (compositional layering) and S_1 (flattening sub-parallel to S_0) are preserved in some cases where lithology and lack of pervasive S_2 permit. S_3 fabric locally kinks S_2. The range of sample grade from this field area encompasses garnet-zone, staurolite-zone, sillimanite-zone, migmatite-zone and garnet + cordierite-zone samples. The typical matrix mineral assemblage is Qtz + Bt + Ms + Plg + Grt + Ilm ± Chl ± St ± Sil ± Rut.

Samples prefixed with TM- are described fully in Menard (1991) and Menard and Spear (1993, 1994). These samples are a series of pelites from the core and/or flanks of the Strafford Dome, central Vermont, and belong to the Devonian Gile Mountain Formation and/or the Siluro-Devonian Waits River Formation (Doll, 1943; Hadley, 1950; Rolph, 1982; Annis et al., 1983). The earliest deformational fabric visible in the TM samples is an S_1 schistosity that is commonly parallel to compositional layering S_0. S_1 is variably crenulated and deformed by F_2, creating an S_2 schistosity (Menard and Spear, 1993). Sample grade ranges from garnet zone to staurolite-kyanite zone. The bulk composition of the TM samples is sufficiently calcic to stabilize epidote in all but one sample (TM-549) and epidote + titanite in one sample (TM-445).

Samples prefixed with V- are from the Valhalla Metamorphic Core Complex, British Columbia, Canada. The Valhalla Complex is one of several exposures of fault-bounded, high-grade metamorphic core complexes that constitute the Shuswap Complex (Armstrong, 1982; Brown and Read, 1983). Several samples from the Valhalla Complex (including V-6 and V-7) display a strong planar fabric defined by aligned biotite and sillimanite, ribboned quartz, and

grain-size-reduced and/or lozenged garnet (Spear and Parrish, 1996). Spear and Parrish (1996) interpret this fabric as a high-temperature shear fabric imparted to the samples near peak metamorphic conditions. Samples V-6A and V-7C are migmatitic pelitic gneisses that experienced peak P-T conditions in the region of 820±30 °C, 0.8±0.1 GPa (Spear and Parrish, 1996). The typical matrix assemblage of these samples is Grt + Bt + Sil + Plg + Qtz + Ilm ± Rut.

Analytical procedures

A large number (> 100) of representative samples from the three field areas were examined with the petrographic microscope under reflected and transmitted light and twenty-nine samples with appropriate accessory phase assemblages and well-characterized major-phase reaction histories were selected for further petrographic and compositional analysis using the JEOL 733 Superprobe at Rensselaer Polytechnic Institute. Accessory phases were identified using back-scattered electron imaging (BEI) and energy-dispersive spectroscopy (EDS). Element distribution maps of Sc, P, Y, Ti, and Cr were collected with the automated mapping program Xraymap, coded by F. Spear and D. Wark. Operating conditions for map collection include an accelerating voltage of 15 kV, Faraday cup current of 1.5-2.0 μA, step size of 5-10 μm/pixel, and dwell times of 0.05-0.1 msec/pixel. Maps were processed with the public domain program NIH Image v. 1.61b12 (Rasband, 1997). Quantitative analyses of Na, Sc, P, Y, Ti, and Cr utilized a ZAF matrix correction routine. Analyses were calibrated on natural and synthetic silicate and oxide standards for Na, Ti, and Cr, and on synthetic phosphates for Sc, Y, and P (Jarosewich and Boatner, 1991). Faraday cup currents for quantitative analysis averaged 500 nA, with 20 sec counting on peak, and 20 sec on background. Baseline and window width were set using pulse-height analysis to minimize second- and higher-order reflection peak interference, and background positions were set to minimize major-element peak interference. For standards, element peaks, baseline, window width, and background positioning used in calibration and quantitative analysis, see Pyle and Spear (1999a). The EMP trace element detection limit (ca. 100 ppm) was calculated using detectability limit equations found in Goldstein et al. (1984). Trace element spot analyses given herein represent the average (in ppm) of five (unless otherwise noted) spot analyses collected in a region of approximately 400 μm^2 (20x20 μm), with values in parentheses showing the standard deviation of the average concentration. Mineral and component abbreviations are from Kretz (1983).

Results

Xenotime distribution

Common accessory phases in the samples studied include xenotime, ilmenite, rutile, Fe-sulfides, apatite, zircon, and monazite (Table 1). Of the twenty-nine garnet-bearing samples examined with BEI and EDS, eighteen contain xenotime. With one exception (sample 92-53), xenotime is subordinate to monazite and/or zircon. Xenotime occurs as subhedral to anhedral grains from <5 μm to approximately 30 μm in diameter. In two samples (93-19A, BF-14P), xenotime occurs as epitaxial overgrowths on zircon. Additionally, xenotime occurs as inclusions in apatite in one sample (BF-17A). Three texturally distinct xenotime habits are noted (Table 1), and described fully below.

The most common habit of xenotime observed in these samples is as inclusions in garnet (Fig. 1). In most cases, xenotime is included in the core section of the garnet, though in two anatectic samples (BF-9H and BF-14P) xenotime occurs as single grains or grain aggregates of near-rim inclusions (Fig. 2), in addition to occurring as core inclusions. Xenotime inclusions in garnet, along with zircon, monazite, and apatite inclusions in garnet, are found at all grades studied. Xenotime is also included in quartz (BF-14P, BF-78) and biotite (93-19A, Fig.3).

Matrix xenotime (habit #2) is texturally unrelated to garnet, and is subordinate in occurrence to xenotime that is included in garnet. Matrix xenotime has been detected in five garnet-bearing samples, BF-15A (garnet zone), 93-19A (garnet-zone, Fig. 3), TM-445 (staurolite zone), BF-14P (migmatite zone), and BF-9H (migmatite zone). Xenotime is particularly abundant in both samples BF-15A and 93-19A (between 0.1 and 0.5 modal per cent), but is not at all abundant in TM-445 (one matrix grain of xenotime was located in this sample); none of the above three samples contain inclusions of xenotime in garnet. The occurrence of xenotime in samples BF-14P and BF-9H is bimodal (xenotime inclusions in garnet and matrix xenotime), and this textural feature is most likely related to the occurrence of melting (and melt-crystallization) reactions in these two samples. Overall, in garnet-bearing samples, matrix xenotime is most abundant in low grade (garnet-zone or below) samples.

The third distinct xenotime habit is the occurrence of xenotime in reaction zones spatially associated with garnet (Fig. 4). Xenotime occurs as inclusions in grains of chlorite or biotite that rim and/or cross-cut garnet (Fig. 4a). Sample 92-53 (garnet zone) contains muscovite-rich pseudomorphs after garnet; several of these pseudomorphs are rich in xenotime inclusions (Figs. 4b, c). Reaction-zone xenotime associated with chlorite, biotite, and muscovite has been found in garnet- and staurolite-zone samples. Xenotime texturally associated with muscovite (± staurolite) adjacent to garnet rims occurs locally in anatectic sample BF-14P.

$[Y]_{Grt}$ and zoning as a function of metamorphic grade

Major and trace element distribution maps (Fe, Mg, Mn, Ca, Na, Sc, P, Y, Ti, Cr) were collected for garnets in twenty-three of the samples studied with BEI, and the mapped garnets were calibrated against quantitative analyses for the above elements (Table 2). Whereas the focus of the present communication is on the significance of Y zoning, selected major element maps and other trace element maps are presented in this section for comparison.

The samples examined in this study are classified in one of five groups, corresponding to the *highest* grade attained by the sample: garnet zone, staurolite zone, sillimanite zone, migmatite zone (presence of melt inferred by leucosomes, symplectites, or other textural features described in Spear et al., 1999), garnet + cordierite zone. Considerable work has been published on these samples for the purpose of determining the dominant reactions responsible for garnet growth and the P-T significance of these reactions (Spear et al., 1990, 1995, Kohn et al., 1992, 1997, Spear and Kohn, 1996, Menard and Spear, 1993, 1994). To place the Y zoning in the context of the major phase parageneses, therefore, the reaction histories are discussed along with the element zoning maps.

Garnet zone. Figure 5 shows a series of garnet Y distribution maps from garnet zone samples 93-19A, TM-549, and PUT-92C2. Sample 93-19A contains matrix xenotime, TM-549 contains inclusions of xenotime in garnet, and xenotime was not identified in sample PUT-92C2. Garnets in all three samples contain a high yttrium core of variable width. It extends to the rim of 93-19A, but drops off about 2/3 of the distance towards the rim in TM-549, and is of limited extent in garnets B and C from PUT-92C2. Garnet A, PUT-92C2 has no high-Y core; this may have resulted from a non-center cut, or later nucleation, as all four PUT-92C2 garnets have broadly the same post-core zoning pattern. The PUT-92C2 garnets also possess rims that are enriched in Y with respect to the outboard portion of the garnets. Overall, the general trend in garnets in garnet-zone samples is a core-to-rim decrease in Y, though some garnet-zone garnets, including PUT-92C2, show an increase in Y away from the core. In an attempt to obtain central-section garnet maps, the largest garnet in each thin section was mapped; however, this did not guarantee a garnet center section as does the application of X-ray tomography (Chernoff and Carlson, 1997b).

The dominant garnet producing reaction in these garnet zone samples is

chlorite + quartz = garnet + water (1)

Major element zoning maps for sample PUT-92C2 (Fig. 6) show element distributions typical of low-grade pelitic garnets. Mn and Ca decrease smoothly outward from the core (Figs. 6d, e), and Mg and Fe (Figs. 6c, b) remain approximately constant throughout a large radial percentage of the garnet, then increase slightly towards the rim. In this sample, yttrium behaves somewhat like Mn and Ca in its decrease towards the rim, but the depletion of Y occurs over a much smaller radial increment. In addition, the rim of the garnet records two distinct yttrium zones: a low-Y zone (~200 ppm) of approximately 30 μm width followed by a high-Y zone (~1300 ppm) approximately 50 μm wide that extends to the garnet rim (Fig. 6a). The formation of the high-Y rim is most likely due to late-stage resorption of garnet, an event that is not well represented in the major-element zoning.

Staurolite zone. Two zoning types are observed in staurolite-zone samples. Many samples contain garnet that displays zoning similar to garnet-zone garnets, characterized by high-yttrium cores of variable width, and zoning shoulders of variable slope. Garnets in staurolite-zone samples also show varying degrees of resorption; this resorption truncates portions of Y-rich garnet in samples BF-57B and BF-18C.

The second zoning type is characterized by narrow (20-300 μm) bands, or annuli, of high yttrium concentration relative to surrounding garnet (Fig. 7). The yttrium content of these annuli varies between 3 and 10 times the yttrium concentration in garnet adjacent to the annulus and the compositional gradient is generally steeper on the inside of the annulus than on the outside. The boundary shapes of Y annuli vary from sharp and euhedral (Fig. 7a) to subhedral (Fig. 7b) to rounded and anhedral (Fig. 7c). A similarly zoned garnet from a staurolite zone sample from Connecticut (Lanzirotti, 1995) contains garnet with euhedral Y annuli.

Locally, annuli are truncated against garnet rims, or are cross-cut by chlorite- or biotite-filled fractures. In some instances, enough of the annulus remains that a pre-truncation annular

reconstruction may be made (Fig. 8). The Y annulus in sample BF-38 is subhedral, and broadly mimics the orientation of the garnet rim (Fig. 8b). Examination of the rim of this garnet (Fig. 8c) reveals that xenotime inclusions in rimming biotite (which truncates the annulus) lie inside the region of the projected annulus. Such xenotime grains are classified as “reaction-zone” xenotime; in this case, yttrium for xenotime growth was furnished by a later period (i.e. post-annulus formation) of garnet consumption that consumed the Y-enriched annular portion of the garnet, and produced biotite.

The first appearance of staurolite in these pelites is caused by the garnet-consuming reaction

garnet + chlorite + muscovite = staurolite + biotite + quartz + water (2)

This reaction proceeds until chlorite is exhausted, consuming garnet and producing staurolite and biotite. Forward modeling of this reaction for typical pelitic bulk compositions (Spear et al., 1991) indicates that the reaction goes to completion (exhaustion of 10-15 vol % of chlorite) over a short temperature interval, approximately 5-8 °C for the assemblage modeled above. Once chlorite is exhausted, garnet growth resumes through a continuous KFMASH reaction

staurolite + biotite = garnet + muscovite + water (3a)

Finally, late biotite (which rims garnet and truncates Y annuli; Fig. 8c) forms by retrograde hydration of the rock

garnet + muscovite + water = biotite + chlorite + quartz (3b)

Figure 9 shows element distribution maps for staurolite-zone sample BF-87A. Fe, Mg and Mn all display smooth zoning (Figs. 9b, c, d), but Ca distribution shows a slight discontinuity near the core (Fig. 9e). Yttrium garnet distribution, as is characteristic of several staurolite zone samples, shows annular structure (Fig. 9a). The inner edge of the annulus corresponds to the break in Ca zoning (Fig. 9e), but there is no high-Y zone in the garnet corresponding to the high-Ca zone outside of the garnet core (Fig. 9e). Given the correspondence between sample grade (staurolite zone) and yttrium annulus occurrence, it is believed that the annulus serves as a marker for consumption of garnet during initial staurolite growth (reaction 2), and subsequent resumption of growth during staurolite consumption (reaction 3). Quantitative analysis of the mechanism of annulus formation follows in the discussion section.

Sillimanite zone. Examination of sillimanite-zone garnets reveals markedly different Y concentrations (Fig. 10). All three samples shown in Figure 10 contain xenotime as garnet inclusions; however, the yttrium content of these garnets is significantly lower than that of xenotime-bearing garnet in garnet- and staurolite-zone samples. Core values for $[Y]_{Grt}$ in xenotime-bearing samples vary between 532 and 182 ppm Y, and the overall variation in $[Y]_{Grt}$ in the same samples is between approximately 620 ppm Y and 120 ppm Y. As a result, Y zoning in garnet is much less pronounced in sillimanite-zone samples than is found in lower grade samples. Examples of both core-to-rim decrease (Figs. 10a, b) and core-to-rim increase (Fig. 10c) in $[Y]_{Grt}$ are observed in sillimanite-zone samples.

The core-to-rim increase in Fe and Ca and decrease in Mn in one sillimanite zone sample (89-22B, Fig. 11) follow a pattern similar to Y zoning. All of these elements display truncation along the lower left side of the crystal, suggesting growth was not radially symmetric. Embayments along the left margin of the garnet grain were originally interpreted (Spear et al., 1995) to have resulted from garnet resorption, but our current interpretation suggests that the embayments are growth features, resulting from pinning of garnet grain boundaries adjacent to quartz.

Spear et al. (1995) interpreted garnets from these samples to have experienced an episode of high temperature homogenization followed by growth via

biotite + sillimanite = garnet + muscovite (4)

Garnet grows along the cooling path in this vapor-absent reaction. Diffusional modification of the rim was concluded to have been insignificant. Inasmuch as garnet Y concentrations in the presence of xenotime appear to decrease with increasing temperature (see above and Pyle and Spear, 1999a), the steady increase in Y zoning towards the rim in the presence of xenotime is consistent with the growth history deduced from the major elements.

As at least one episode of garnet resorption followed by renewed garnet growth has occurred in sillimanite-zone rocks, the absence of Y annuli (as seen in staurolite-zone garnets) is notable. The garnet shown in Figure 10b appears to be a candidate for a sillimanite-zone garnet with a Y annulus. However, discontinuities in garnet Y zoning are sharp in migmatite-zone samples, which suggests that Y diffusion in garnet is slow, and that Y discontinuities in garnet are preserved at very high metamorphic grades. If local equilibrium is maintained, renewed garnet growth at $T \geq 600$ °C will produce garnet with a low Y concentration. It is likely, therefore, that garnet in Fig. 10b does not display a Y annulus of the "staurolite-zone" type, but instead records down temperature garnet growth, with a concomitant, equilibrium, increase in $[Y]_{Grt}$.

Migmatite zone. Sample BF-14P is a representative migmatite-zone sample that contains two texturally distinct garnet habits: large (up to 1 cm across) porphyroblastic, anhedral crystals; and smaller (0.025-0.25 mm), idioblastic crystals (Spear et al., 1990). The large garnet crystals are interpreted as early nucleates and have undergone up to five periods of growth, sometimes with intervening periods of resorption (Kohn et al., 1997). The small garnet crystals nucleated later and experienced only one or two periods of growth. Evidence for resorption in the second-generation garnets in sample BF-14P is equivocal.

Element distribution maps for Sc, Cr, Y, and P in a large early garnet (Fig. 12) reveal: (1) a modest core [Y] concentration (1059 ppm) that decreases towards the rim (Fig. 12c); (2) an annulus that is enriched in Sc and Cr (Figs.12a, b) relative to the core and slightly enriched in Y (1245) and also displays oscillatory zoning (Fig. 12c); (3) a sharply discontinuous zone of depleted Sc, Cr, and Y just outboard of the annulus; (4) a largely homogeneous P distribution across the entire garnet (Fig. 12d).

Spear and Kohn (1996) and Kohn et al. (1997) have examined garnets in samples from the same outcrop, and conclude that the loss of muscovite by the reaction

muscovite + quartz + plagioclase = sillimanite + K-feldspar + melt (5a)

followed by the loss of biotite and growth of garnet by the reaction

biotite + sillimanite + plagioclase + quartz = garnet + K-feldspar + melt (5b)

during up-temperature vapor-absent melting, produced a generation of garnet enriched in chromium with respect to pre-anatectic garnet. Presumably, Cr was sequestered in muscovite prior to melting, after which it partitioned strongly into biotite, and then into garnet upon biotite melting (Spear and Kohn, 1996).

Comparison of major and trace element zoning patterns (Fig. 13) reveals sharp discontinuities in trace element zoning compared to major element zoning profiles. Zoning of Fe, Mg and Mn (Figs. 13c, d) have all been modified substantially by diffusion at high temperature, driven by the garnet consuming net transfer reaction (5b) progressing from right to left upon crystallization of the melt. (See Spear and Florence, 1992, for a diffusion model and major-element zoning profiles of garnet from sample BF-14P. Note, however, that in that paper the retrograde reaction was assumed to be a hydration reaction rather than a crystallization reaction). This apparent contrast in major/trace element diffusional modification attests to the considerable difference in diffusivities between Fe, Mg, Mn and trace elements. The Ca-discontinuity between non-anatectic garnet ("1" in Fig. 13b) and anatectic garnet ("2" in Fig. 13b), outlined clearly on the Y map (Fig. 13a), is quite diffuse (Fig. 13b). The slight increase in X_{grs} (~2 mole%) indicates that the muscovite melting reaction occurred at a pressure close to (and above) the KFMASH invariant point at the intersection of the muscovite dehydration reaction and the H_2O-saturated pelite solidus (Spear and Kohn, 1996). Zones "3" and "4" (Fig. 13b) indicate garnet that grew at temperatures of roughly 625 °C and 500 °C, respectively (Kohn et al., 1997)

Garnet-cordierite zone. The highest grade New England samples come from the garnet-cordierite zone in central New Hampshire. These rocks are from the highest structural level (the Chesham Pond nappe) and experienced higher peak metamorphic conditions of 700-730 ˚C, 0.2-0.4 GPa).

Major element zoning in these samples has been completely homogenized by diffusion near the metamorphic peak (Fig. 14b-e). Cores were homogenized during and rims were zoned in response to retrograde progress of reaction (5b). In contrast, Y zoning preserves garnet growth (Fig. 14a). Xenotime inclusions are found in the garnet core and Y zoning resembles the type of zoning observed in garnet zone samples (e.g. Figs. 5 and 6).

Discussion

The images presented in the sections above reveal a number of important observations regarding the distribution of trace elements, especially Y, in garnet. In the next section we present a brief discussion of the correlation between xenotime distribution and $[Y]_{Grt}$, and present models for (1) Y distribution in xenotime-absent garnet, (2) annulus formation, and (3) high-temperature enrichment of $[Y]_{Grt}$ in anatectic samples.

Correlation between xenotime distribution and $[Y]_{Grt}$.

For all garnets that contain xenotime inclusions, and that occur in or below the sillimanite zone, the portion of the garnet with the highest yttrium concentration corresponds to the location of the xenotime inclusions. The correlation is especially dramatic in BF-17A (Fig. 15a). Xenotime grains are restricted to garnet cores, and the location of the xenotime grains defines a very high-Y (~5000 ppm) region in the garnet that is sharply separated from the outboard region of garnet where concentration of Y is below EMP detection limits (<100 ppm, Fig. 15a). Similarly, garnet cores with xenotime inclusions generally contain more Y than garnets without xenotime inclusions.

The high-yttrium-in-garnet correlation does not apply to other phosphate minerals. Figure 15b shows a Y map scaled to show only the garnet core in sample BF-17A, which clearly shows that xenotime inclusions are restricted to the high-Y core. A map of phosphorous distribution (Fig. 15c) in the same garnet reveals numerous phosphates (apatite and monazite) throughout the garnet outboard and in the matrix. These observations imply that xenotime reacted out after the growth of the high-Y garnet core and before the growth of the low-Y garnet rim. In contrast, examination of garnet Y distribution for samples with matrix xenotime suggests that xenotime was present throughout the entire growth history of garnet. Sample 93-19A (Fig. 15d) contains matrix xenotime and garnet that is smoothly zoned in yttrium, from a value of ~2150 ppm Y in the core to ~1500 ppm at the garnet rim.

These observations permit assessment of the assignment of equilibrium criteria to coexisting garnet and xenotime. If xenotime is present only as inclusions in garnet, we infer that only the garnet core grew in close approach to equilibrium with xenotime. In the case of BF-17A (Figs. 15a, b), xenotime is restricted to the garnet core, and equilibrium between garnet and xenotime is assumed only for the core portion of the garnet. In sample BF-14P (Figs. 2 and 12), xenotime occurs as both core inclusions and as aggregates of small crystals near the garnet rim, so equilibrium between garnet and xenotime is inferred for both the core and the near-rim regions of garnet, but not for the region of high-Y annulus (Fig. 12b), where no xenotime occurs. The yellow phases included in the anatectic region of garnet are grains of ilmenite; one grain of apatite (Fig. 12d) occurs between two high-Y bands in the lower left portion of the garnet (Fig. 12d). In the case of matrix xenotime, equilibrium between garnet and xenotime is assumed to apply throughout the growth history of the entire garnet *as long as no discontinuities in garnet Y zoning are evident* (e.g. sample 93-19A, Fig. 15d). Lastly, xenotime in reaction zones spatially associated with garnet is inferred *not* to be in equilibrium with garnet, having been formed through retrograde reactions that consume garnet and produce xenotime ± chlorite ± biotite ± muscovite (e.g. sample BF-38B; Fig. 8 and sample 92-53; Fig. 4c). These criteria help to delineate reaction histories involving garnet and xenotime, and are generally confirmed by the temperature dependence of the equilibrium constant used in calibration of the xenotime-YAG thermometer (Pyle and Spear, 1999a).

In summary, several important conclusions are reached based on these observations:

(1) The form of yttrium zoning in garnet is strongly dependent on the presence or absence of xenotime, and on its distribution (garnet inclusions only vs. matrix xenotime).

(2) There is a strong temperature dependence of $[Y]_{Grt}$ in xenotime-bearing samples, with [Y] decreasing with increasing T (Pyle and Spear, 1999a).
(3) Yttrium distribution in garnet may be a sensitive indicator/recorder of specific events in the reaction histories of pelites that contain Y-enriched accessory phases, such as monazite, titanite, zircon, epidote, and especially xenotime.

Prograde consumption of xenotime

The occurrence of matrix xenotime in lower granulite-facies pelites (Heinrich et al., 1997) and granitic plutons (Wark and Miller, 1993) implies that xenotime has significant thermal stability with respect to regional metamorphic P-T conditions. However, the scarcity of matrix xenotime at grades above the garnet-zone in garnet-bearing pelites implies that the growth of garnet is accompanied by the consumption of xenotime. Garnet is the only major pelite phase that incorporates significant amounts of Y. For example, quartz, biotite and muscovite from the Straits Schist (Connecticut) contain 2-5 ppm Y (quartz) and 200-300 ppm Y (biotite and muscovite) (Lanzirotti, 1995). Biotite and muscovite from four of the samples in this study , and staurolite from sample BF-38, all contain less than 1 ppm Y (Pyle and Spear, 1999b), and the maximum yttrium content of biotites from 27 pelites and quartzofeldspathic gneisses from western Labrador is 2 ppm (Yang et al., 1999). The elevated concentration of Y in biotite and muscovite analyzed by Lanzirotti (1995) is most likely due to accessory phase inclusions. Accessory phases such as zircon (up to 6 wt. % Y_2O_3), monazite (~3 wt. % Y_2O_3), titanite (~1.5 wt. % Y_2O_3), epidote (~1 wt. % Y_2O_3), and allanite (~0.1 wt. % Y_2O_3) (Görz and White, 1970; Deer et al., 1992; Heinrich et al., 1997; Finger et al., 1998) may contain significant yttrium, but these are generally of limited modal extent in comparison to garnet (e.g. <0.1 to 0.5 vol% monazite in the pelites studied). Therefore, as garnet grows in the presence of xenotime in the garnet zone with Y concentrations of several thousand ppm, the Y is supplied by the breakdown of xenotime.

This effect is shown qualitatively in Figure 16 in a pseudo-ternary Fe-Mg-Y diagram. At T_1, garnet in equilibrium with chlorite and xenotime contains an amount of yttrium dictated by the mass action between the three coexisting phases (note that the absolute amounts of Y in both garnet and chlorite are exaggerated for clarity). The EBC (effective bulk composition), however, is dictated by the compositions and modes of xenotime and biotite and plots on the chlorite-xenotime tie-line, as material in the garnet core is chemically isolated from the matrix.

As temperature increases, the Y content of garnet in equilibrium with xenotime decreases (Pyle and Spear, 1999a) and the phase relations shift as shown by the dashed lines (Fig. 16). As garnet grows, Y is removed from the matrix and the EBC moves directly away from the garnet composition (red arrow). At the same time, however, continuous reactions between garnet and chlorite move both phases to lower Fe/(Fe + Mg) values. The net effect of these two changes (removal of Y from the EBC by garnet crystallization and an decrease in Fe/(Fe + Mg) of both chlorite and garnet) is to sweep the 3-phase garnet-chlorite-xenotime triangle past the EBC, and strand the EBC in the 2-phase chlorite-garnet region. At this point, the matrix no longer contains sufficient yttrium to stabilize xenotime, and it disappears from the rock. The remaining yttrium is partitioned largely among garnet and Y-compatible accessory phases (e.g. zircon, monazite, and apatite).

Formation of steep Y zoning profiles

Rayleigh fractionation model. Many garnets in both garnet- and staurolite-zone samples possess the same general yttrium zoning pattern, which consists of a high yttrium core (with xenotime inclusions), followed by a zoning shoulder of variable width, with an outboard region of garnet in which [Y] is below EMP detection limits. Sample BF-58B (Fig. 17a) contains garnet with a 2400 ppm Y core that decreases in Y content over a narrow (~200 μm) zone to an outboard region where the yttrium concentration is below EMP detection limits.

The zoning is consistent with early growth of garnet at an approximately constant activity of yttrium in the sample, followed by disappearance of the Y-buffering phase, and fractionation of remaining available yttrium into the garnet rim. An attempt was made to reproduce the measured garnet zoning profiles using Rayleigh fractionation modeling after the method of Hollister (1966). The measured zoning profiles are modeled with the equation

$$Y_G = \lambda Y_0(1-W_G/W_0)^{\lambda-1}$$

where Y_G is the weight fraction of yttrium in garnet at the garnet rim, Y_0 is the initial (pre-fractionation) weight fraction of the yttrium in the rock, W_G/W_0 is the weight fraction of garnet in the rock, and λ (= $[Y]_{Grt}/[Y]_{bulk\ rock}$) is the bulk fractionation factor between garnet and the bulk-rock reservoir. As an initial constraint, the product of λ and Y_0 is fixed at a constant value of 2100 ppm at the point on the garnet where Rayleigh behavior commences. Fit to the measured zoning profile is optimized by varying λ and Y_0 (subject to the constant product constraint), homogeneous core radius, and rock volume.

A visual best-fit to the measured profile of garnet BF-58B is produced with model values λ = 200 and Y_0 = 10.5 ppm, and a rock volume of 0.008 cm^3 (equivalent to a nucleation density of 125 garnets/cm^3). The model value of Y_0 is consistent with estimates based on modal mineralogy and compositions of pelitic phases. Biotite, muscovite, staurolite, and quartz in the study samples all contain less than 2 ppm Y (Pyle and Spear, 1999b), and Y concentration in chlorite and plagioclase is probably of this order or less. Whole-rock concentration in a typical pelite, exclusive of accessory phases, is therefore on the order of 1-2 ppm. Addition of 0.05 wt. % monazite with [Y] = 13000 ppm (1.65 wt. % Y_2O_3), and ~0.1 wt. % zircon and apatite with [Y] = 1000 ppm each increases the whole-rock yttrium content to approximately 10 ppm Y. These Y concentrations are representative of the above accessory phases (e.g. Pyle and Spear, 1999b; Bea, 1996; Finger et al., 1998), and the resultant Y_0 is in excellent agreement with our model value. Although carrying a high degree of uncertainty, the Rayleigh fraction model appears to provide an excellent fit to the zoning profiles (Fig. 17b).

Diffusion model. An alternative hypothesis to the one presented above involves diffusional modification of a garnet with an initial step function in Y concentration. In principle, extended residence time at peak T conditions could modify this compositional step function, and produce the zoning profile seen in garnet in sample BF-58B.

Diffusion in garnet has been modeled as a one-dimensional extended source of limited extent following Crank (1975, p. 15, eq. 2.15) with the results shown in Figure 17c. The initial

conditions were set at $C_{0,yttrium}$ = 2300 ppm and a visual fit was made to the observed profile values. The slight difference between C_0 for diffusion modeling (2300 ppm Y) and Rayleigh fractionation modeling (2100 ppm Y) maximizes visual best-fit in each model. This procedure yielded an optimal value of $\sqrt{Dt}$ = 3.075x10^{-3} cm. Solving for the value of D requires knowledge of the temperature-time history. The time of peak metamorphism is approximately 390-400 Ma (Eusden and Barreiro, 1988) and $^{40}Ar/^{39}Ar$ ages on hornblende are approximately 350 Ma (Spear and Harrison, 1989). Assuming a diffusion time scale of 25 M.y. for cooling from the metamorphic peak of ca. 560 ˚C to 525 ˚C results in a calculated average diffusivity of D = 1.2 x 10^{-20} cm^{2}sec^{-1}.

Overall, the diffusional model fit to the measured zoning profiles is as good as the Rayleigh fractionation fit, but it is not believed that the zoning profile is the result of diffusional relaxation of an original step function. At a similar temperature (560 ˚C), the value for the tracer diffusion coefficient of Mn in garnet (D^*_{Mn}) is 4.3x10^{-20} cm^{2}sec^{-1} (Chakraborty and Ganguly, 1992), which is of the same order of magnitude as the inferred diffusivity of Y in garnet. In higher grade samples (e.g. migmatite zone sample BF-14P), however, Mn has diffused over a length scale of approximately 1 mm whereas Y (and Cr) zoning in the same garnet crystal is sharp and cannot have diffused over length scales greater than approximately 10 μm. Based on the retention of zoning discontinuities preserved in high-grade anatectic garnets, Y (and Cr) diffusivity must be at least 4 orders of magnitude slower than Mn diffusivity in this sample. Sc zoning in garnet also preserves compositional discontinuities in anatectic garnet, but does not retain the fine-scale oscillatory zoning seen in the Y element map (Figs. 12a, c), suggesting that Sc diffusivity in garnet is intermediate to the diffusivities of Y and (Fe, Mg, Mn) in garnet. This observation has also been noted in garnets from micaceous quartzite of the Picuris Range, New Mexico (Chernoff and Carlson, 1999).

Our favored interpretation, therefore, calls on Rayleigh fractionation as responsible for formation of the steep yttrium zoning profiles observed in samples such as BF-58B (Fig. 17).

Formation of high-yttrium annuli in staurolite-zone samples

A particularly interesting feature in the present sample suite is the occurrence of high-yttrium annuli in garnet interiors (e.g. Figs. 7 and 8). Although high-yttrium rims have been observed in garnet-zone samples (e.g. Fig. 6, sample PUT-92C2), the annuli are restricted in our population to samples from the staurolite zone or higher grades. Therefore, we seek an explanation for the formation of these annuli that are a natural consequence of the prograde metamorphism of pelites.

Staurolite is formed in the low-Al pelites of the sample suite by reaction (2):

garnet + chlorite + muscovite = staurolite + biotite + quartz + water (2)

In this reaction, garnet, muscovite, and chlorite are consumed until (a) one of the reactants disappears, or (b) kinetic considerations (e.g. decreasing T) force cessation of the reaction. In the case of (a) in typical pelite bulk compositions, exhaustion of chlorite will terminate progress of (2). The amount of garnet consumed (i.e. total mass) is a function of the mode of chlorite, but the

radial increment of garnet consumed is a function of the size of garnet crystals in the rock (i.e. the nucleation density of garnet). That is, for an equal volume (or mass) of garnet consumption, smaller garnet crystals will lose a larger radial increment than will larger crystals. Once chlorite is consumed, garnet growth follows via continuous KFMASH reactions such as (3):

staurolite + biotite = garnet + muscovite + water (3)

During the consumption of garnet in reaction (2), yttrium from the consumed garnet is released into the matrix, raising the activity of yttrium in the environment. If local equilibrium prevails during garnet consumption, the yttrium released will be distributed among matrix phases. Inasmuch as monazite (nearly ubiquitous in these samples) can harbor the highest Y concentration next to xenotime, growing monazite is a likely sink for this yttrium. Biotite and staurolite in these samples contain ≤ 2 ppm Y, and will not incorporate Y to a great degree. If yttrium activity rises to a sufficiently high value, then xenotime may form. The re-distribution of Y upon garnet consumption is markedly different from Mn re-distribution, where lack of an Mn-incorporating phase combined with diffusive transport of Mn back into the garnet enriches the garnet rim in Mn relative to the garnet just inside the rim (e.g. Spear et al., 1991). Examples of the formation of xenotime (or Y-bearing monazite) from garnet resorption are common during late replacement of garnet by chlorite or biotite (e.g. Figs. 4 and 8). A particularly revealing example is shown in Figure 18, in which the resorption of garnet by reaction (2) has been arrested. Furthermore, if local equilibrium prevails, the concentration of yttrium on the rim of the garnet should increase to reflect the increased Y activity in the matrix. Resumption of garnet growth will occur in this environment of higher Y activity, and garnet produced by reaction (3) will have higher Y concentration, resulting in the formation of an annulus. If xenotime has been stabilized, the annulus will have a relatively constant composition at high Y value until xenotime is again depleted. No examples of xenotime re-saturation were observed in the present sample suite, but the high Y annulus described by Lanzirotti (1995) is a probable example. After xenotime is depleted (or if it was never stabilized), Y concentration in garnet will fall off according to the Rayleigh fractionation model.

If the above model is correct, then mass balance calculations can be used to estimate the amount of garnet that has been consumed by reaction (2). Assuming that a pre-staurolite garnet had a initial radius of r_0 and an initial near-rim Y concentration of $C_{Y,0}$, and that during staurolite growth the garnet was consumed concentrically down to a radius of r_c, the amount of yttrium released to the matrix from this homogeneous region of garnet is given by

$$m_{Y,0} = C_{Y,0} \times \frac{4\pi}{3}\left(r_0^3 - r_c^3\right)$$

Upon renewed garnet growth, this identical mass $m_{Y,0}$ is incorporated into the high Y annulus. The total mass of Y contained in the annulus can readily be calculated from the zoning profile:

$$m_{Y,0} = \sum_{j=1}^{n} C_j \times \frac{4\pi}{3}\left(r_j^3 - r_{j-1}^3\right)$$

Equating the above two equations and using the radius of the inside of the annulus for r_c allows calculation of the pre-staurolite radius of garnet (r_0):

$$r_0 = \left(\frac{m_{Y,0}}{C_{Y,0}} + r_c \right)^{\frac{1}{3}}$$

An example of this calculation is given in Figure 19. The yttrium concentration of this garnet is approximately constant for ca. 0.2 mm towards the rim of the high-Y core (Fig. 19a). The pre-staurolite $[Y]_{Grt}$ is taken as the average of the constant-composition increment from point 1 to point 2 (588 ppm Y), where point 2 is interpreted to mark the limit of garnet resorption during the progress of reaction (2). Balancing the mass under the annulus (dotted line in Fig. 19b) under the assumptions outlined above, requires that a radial increment of 0.267 mm was consumed during staurolite growth. This estimate results in a postulated rim position 0.043 mm inside the present petrographic rim, and a volumetric consumption of approximately 70% of the original garnet, but with second-generation growth producing a garnet of slightly larger size.

The calculated pre-staurolite garnet rim in this example lies just inside of the present rim, rendering it unlikely that petrographic evidence for garnet resorption has survived. However, inasmuch as it is unlikely that all garnets in a sample will have been consumed and regrown by exactly the same amount, evidence for garnet resorption might be found in some garnets from the sample. A likely example is shown in Figure 20, which is a cathode luminescence image of another garnet from the same sample. The image shows clearly that quartz in the vicinity of the garnet rim (yellow arrow in Fig. 20) has a different luminescence than quartz further from the rim (black arrow in Fig. 20). Reaction (2) produces quartz, and it is postulated that the quartz produced during consumption of this garnet was deposited locally around the garnet rim. Minor differences in the trace element composition of quartz produced from reaction (2) are the likely cause of the luminescence contrast.

Other mechanisms for annular rings of high Y in garnet have been proposed. For example, Lanzirotti (1995) lists a number of possible mechanisms including (1) open system-fluid infiltration; (2) garnet resorption and renewed growth (our preferred mechanism); (3) changes in garnet growth rates; and (4) breakdown of Y-enriched phases. Fluid infiltration is a possible mechanism and has been employed by Stowell et al. (1996) to explain oscillatory zoning of Ca, Fe, Na, Y, Yb, Zr, and Ti in zoned garnets from contact aureoles surrounding plutons in the Grand Island (Alaska) diorite complex. However, it is not a likely explanation for the present samples because it does not explain why only samples from the staurolite zone and above display annuli. Breakdown of Y-enriched phases is known to occur throughout garnet growth (e.g. xenotime breakdown) but there is no phase equilibrium reason why this should produce an annulus (in the absence of additional kinetic arguments).

Kinetic mechanisms warrant further discussion. Lanzirotti (1995) suggested that if the supply of Y to the growing garnet interface is diffusion-limited in the matrix, then a decrease in the

garnet growth rate will result in an increase in the supply of Y and a corresponding increase in $[Y]_{Grt}$. A similar argument was used by Welch and Tracy (1998) to explain Y annuli in a polymetamorphic garnet from the Gassetts Schist (Vermont).

Alternatively, kinetic control of partitioning at the garnet rim can affect $[Y]_{Grt}$. Trace element concentrations are known to be enriched in the interfacial regions of polycrystalline aggregates (Kingery, 1984; Watson, 1996). The concentration anomaly may arise from existence of lattice strain near grain or interphase boundaries that creates distorted lattice sites favoring occupation by impurities at a distance of many monolayers from the interphase boundary itself. Li and Kingery (1984) estimate that the concentration anomaly may extend into the grain as far as 20 nm from the interface. If garnet growth is rapid, the high-Y interface region can be overrun by crystal growth, and, in essence, successive interface layers are stacked, preserving the compositional anomaly (e.g. Watson, 1996). Hickmott and Shimizu (1990) used this argument to explain Ti zoning in garnet from a contact aureole from the Kwoiek area, British Columbia.

Chernoff and Carlson (1997a, 1997b, 1999) presented yet another kinetic model to explain trace element and Ca spikes in garnet zoning profiles in rocks from the Picuris range, New Mexico. Under the assumption that the MnO content of garnet is a time marker (identical garnet core concentrations of MnO = identical nucleation time), they concluded that Ca and trace element spikes cannot represent a single rock-wide event, as there is a wide range of MnO values at Ca and trace-element spikes in different garnets. Instead, Chernoff and Carlson (1997a, 1997b, 1999) postulate that impingement of multiple “depleted zones” around growing garnet porphyroblasts releases material (e.g. Ca or Y) from transient mineral sinks in an intermediate reaction zone. As material diffuses from the reactant phase toward garnet, it is temporarily stored in a transient mineral sink. In this case, accessory phases such as REE phosphates, REE silicates (e.g. allanite, titanite) or zircon are potential sinks. In response to diminished matrix flux from the original reactant of the element of interest (which occurs as the reaction nears local completion), the transient sink becomes locally unstable, and converts to a source. Conversion from sink to source is the local supply for the elemental spike in the garnet porphyroblast.

While the validity of these models is not questioned here, and their operation may occur in specific geologic environments, kinetic models are not believed to explain the Y annuli observed in the present sample suite. Our principal argument in favor of a phase equilibrium explanation (i.e. garnet consumption by reaction 2, followed by garnet growth upon exhaustion of chlorite) is the observation that the annuli do not occur in simple pelites (i.e. pelites without epidote, allanite, or titanite) in which a garnet-consuming reaction has not occurred (i.e. low grade rocks below the staurolite isograd). This observation is also valid for the staurolite-bearing rock studied by Lanzirotti (1995).

Formation of trace-element annuli involving garnet growth processes exclusively has been hypothesized by a number of workers (e.g. Lanzirotti, 1995; Chernoff and Carlson 1999). These workers cite the euhedral outlines of such trace element annuli as evidence for formation of annuli without a hiatus in garnet growth; such a hiatus (i.e. due to garnet resorption) would be expected to produce an irregular, embayed garnet margin. Renewed garnet growth on an irregular boundary should produce a subhedral to anhedral annulus. The majority of Y annuli preserved in garnets in our study set differ greatly from those observed by Chernoff and Carlson

(1999) in that instead of euhedral outlines, our annuli display subhedral or even anhedral outlines (Figs. 7b, c; Fig. 8), which indicate garnet resorption prior to garnet growth. One sample which *does* display a euhedral annulus (TM-445, Fig. 7a) has a different reaction history than BF-38 and BF-64. It is believed that the Y annulus in TM-445 is a result of a titanite-out reaction, as titanite is restricted to the garnet core inwards of the Y annulus. It should be noted that production of such an annulus – without garnet resorption – requires that the accessory-phase-out reaction be essentially discontinuous, or the result would be a gradual, rather than abrupt, increase in garnet trace-element content.

Although garnet resorption is generally accepted to produce anhedral garnet margins (e.g. Spear et al., 1995), textural evidence for euhedral garnet consumption is present in TM-637 (Fig. 18a). A lineation of ilmenite + biotite 300-500 μm from the garnet rim almost perfectly mimics the shape of the garnet rim, and several garnets in this sample possess high-Y rims, which may have been formed during growth of garnet + kyanite at the expense of staurolite and chlorite (Menard and Spear, 1993, 1994). Whether garnet trace-element annuli form during hiatus-free garnet growth, or garnet-growth following resorption, it is clear that examination of whole-rock reaction history (including both major and accessory phases) may elucidate the most likely reaction responsible for equilibrium formation of the annulus, if kinetic arguments for annulus formation are unwarranted.

Yttrium enrichment in garnet from anatectic pelites

Calibration of the xenotime-YAG thermometer (Pyle and Spear, 1999a) has shown that there is a strong temperature dependence of yttrium content in garnet in xenotime-bearing samples. In xenotime-bearing samples, $[Y]_{Grt}$ decreases from approximately 5000 ppm in the lower garnet zone to less than 100 ppm in high-grade samples V6B and V7D, which experienced peak metamorphic conditions of approximately 0.8 GPa and 820 °C (Spear and Parrish, 1996).

However, an apparent contradiction to this trend is observed in samples BF-14P and K92-12D, both of which are from the migmatite zone in western New Hampshire. In these samples, Y concentrations in the parts of garnet that grew in the presence of a melt phase by reactions (5a,b) are >1000 ppm (i.e. 1245 ppm in sample BF-14P, Fig. 21). Inasmuch as xenotime is not present over this interval of garnet growth, it would be expected that $[Y]_{Grt}$ should be lower than that predicted by the xenotime-YAG thermometry at the inferred temperature of 700-730 °C (i.e. <100 ppm).

The apparent paradox is resolved by the recognition that the stability of xenotime depends not only on the activity of Y but also on the activity of PO_4 in the sample. A careful search of the anatectic garnet in samples BF-14P and K92-12D (indicated by the high Cr zones; Figs. 12 and 21) revealed the absence of phosphates included in garnet. In sample BF-14P (Fig. 21), garnet contains monazite, apatite, and xenotime as core inclusions. In the high Y/Cr/Sc zone (outlined in white in Fig. 21c), phosphates are present only as inclusions in ilmenite. Phosphates (specifically xenotime) are again present in the outermost rim of the garnet, which is interpreted to have grown during retrogression of biotite + sillimanite assemblages, after melt has crystallized (Kohn et al., 1997). The same textural relationships hold in sample K92-12D (a

xenotime-absent sample): apatite and monazite are present in the low-Cr garnet core and outboard, but absent from the high-Cr region that grew during biotite-dehydration melting.

The implication of this observation is that all available phosphate had dissolved into the melt, lowering the activity of phosphate below that for phosphate saturation. If the phosphates apatite, monazite, and xenotime are removed from the assemblage by dissolution into the melt, garnet (and possibly zircon, e.g. Görz and White, 1970; Wopenka et al., 1996) are the sole remaining phases that strongly fractionate Y and HREE. Bea et al. (1994) report the following garnet-leucosome partition coefficients: $D_Y = 69.2 \pm 1.5$, $D_{Dy} = 72.3 \pm 2$, $D_{Er} = 348 \pm 5$, $D_{Yb} = 331 \pm 4$, all of which indicate the strong affinity of HREE for garnet in equilibrium with peraluminous melts. Therefore, in the absence of phosphate phases, the activity of Y is free to rise, with phosphates suppressed because of reduced phosphate activity. Garnet grown in this environment has a composition that reflects partitioning between garnet and melt and is not constrained by xenotime activity.

Conclusions

The analysis of Y in pelitic garnet suggests that there is an intimate relationship between major and accessory phases during the reaction history of pelitic rocks. In light of this observation, it is posited that any study attempting to explain metamorphic trace element distribution in terms of major phases or accessory phases alone would be incorrect because it would fail to recognize the integrated nature of the phase assemblage interaction. The final trace element distribution recorded by any metamorphic rock is a direct result of the whole rock reaction-history. Each unique (and often simultaneous) reaction progress reflects the modal preponderance of the major phases involved (which exert great control over effective bulk composition and, therefore, mineral stability), but also the presence of trace-element-sequestering accessory-phases (which buffer trace-element activities and/or exert very strong trace-element partitioning control). The major phase - accessory phase coupling during reaction progress will be most profound if: (1) the major phase fractionates material during growth; (2) the major phase has a strong affinity for an element stored largely in an accessory phase.

The slow diffusivity of trace elements in garnet leads to recognition of whole rock events that were either unrecorded by major elements, or were recorded but subsequently erased by high-temperature diffusive re-equilibration. The preservation of these trace-element-flagged events enables reaction-specific calculations – growth or consumption volume of phases, empirical diffusivity fits, forward modeling via the Gibbs method – that cannot be performed on a major-element distribution basis alone. Moreover, metamorphic trace-element distributions allow for a much more complete understanding of whole-rock reactions, and complement existing studies of trace-element geothermobarometry (Pyle and Spear, 1999a; Andrehs and Heinrich, 1998). This study shows that valuable petrogenetic information can be gleaned from exploring trace-element distribution in metamorphic rocks, and that no *complete* understanding of reaction history may be achieved if accessory phases are excluded from investigation.

Acknowledgements

Funding for this research was provided by NSF grants EAR-9706463 and EAR-9903036 (to FSS). We also thank David A. Wark for his assistance with trace-element analyses on the JEOL 733 Superprobe at Rensselaer Polytechnic Institute. Carlotta Chernoff and Toby Rivers are thanked for their insightful, constructive, and highly detailed reviews of an earlier version of this manuscript, and John Brady is thanked for his editorial handling of the manuscript.

References Cited

Andrehs, G., and Heinrich, W. (1998) Experimental determination of REE distributions between monazite and xenotime: potential for temperature-calibrated geochronology. Chemical Geology, 149, 83-96.

Annis, M.P., Slack, J.F., and Rolph, A.L. (1983) Stratabound massive sulphide deposits of the Elizabeth Mine, Orange County, Vermont. In: Sangster, D.F. (ed.) IGCP-CCSS Symposium Field Trip Guidebook to Stratbound Sulphide Deposits, Bathurst Area, N.B., Canada, and West-Central New England, U. S. A. Geological Survey of Canada Miscellaneous Report, 36, 41-51.

Armstrong, R.L. (1982) Cordilleran metamorphic core complexes – from Arizona to southern Canada. Annual Reviews of Earth and Planetary Science, 10, 129-154.

Bea, F. (1996) Residence of REE, Y, Th, and U in granites and crustal protoliths; implications for the chemistry of crustal melts. Journal of Petrology, 37, 521-552.

Bea, F., Pereira, M.D., and Stroh, A. (1994) Mineral/leucosome partitioning in a peraluminous migmatite (a laser ablation-ICP-MS study). Chemical Geology, 117, 291-312.

Brown, R.L., and Read, P.B. (1983) Shuswap terrane of British Columbia: a Mesozoic 'core complex'. Geology, 11, 164-168.

Charkraborty, S., and Ganguly, J. (1992) Cation diffusion in aluminosilicate garnets: experimental determination in spessartine-almandine diffusion couples, evaluation of effective binary diffusion coefficients, and applications. Contributions to Mineralogy and Petrology, 111, 74-86.

Chamberlain, C. P. (1986) Evidence for the repeated folding of isotherms during regional metamorphism. Journal of Petrology, 27, 63-89.

Chernoff, C.B., and Carlson, W.D. (1997a) Trace-element zoning in garnet: evidence for disequilibrium during garnet growth (abstract). Geological Society of America Abstracts with Programs, 29, A-338.

Chernoff, C.B., and Carlson, W.D. (1997b) Disequilibrium for Ca during growth of pelitic garnet. Journal of Metamorphic Geology, 15, 421-438.

Chernoff, C.B., and Carlson, W.D. (1999) Trace element zoning as a record of chemical disequilibrium during garnet growth. Geology, 27, 555-558.

Crank, J. (1975) The Mathematics of Diffusion (2nd edn). 414 p., Oxford University Press, Oxford.

Deer, W.A., Howie, R.A., and Zussman, J. (1992) An Introduction to the Rock-Forming Minerals (2nd edn). Longman Scientific and Technical, London, 696 p.

Doll, C.G. (1943) A preliminary report on the geology of the Strafford Quadrangle, Vermont. Vermont Geological Survey, 24th report of the State Geologist, 14-28.

Eudsen, J.D., and Barreiro, B. (1988) The timing of peak high-grade metamorphism in central-eastern New England. Maritime Sediments and Atlantic Geology, 24, 241-255.

Exley, R.A. (1980) Microprobe studies of REE-rich accessory minerals: implications for Skye granite petrogenesis and REE mobility in hydrothermal systems. Earth and Planetary Science Letters, 48, 97-110.

Finger, F., Broska, I., Roberts, M.P., and Schermaier, A. (1998) Replacement of primary monazite by apatite-allanite-epidote coronas in an amphibolite facies granite gneiss from the eastern Alps. American Mineralogist, 83, 259-272.

Franz, G., Andrehs, G., and Rhede, D. (1996) Crystal chemistry of monazite and xenotime from Saxothuringian-Moldanubian metapelites, NE Bavaria, Germany. European Journal of Mineralogy, 8, 1097-1118.

Goldstein, J., Newbury, D., Echlin, P., Joy, D., Fiori, D., and Lifshin E. (1984) Scanning Electron Microscopy and X-Ray Microanalysis. Plenum, New York, 673 p.

Görz, H. and White, E.W. (1970) Minor and trace elements in HF-soluble zircons. Contributions to Mineralogy and Petrology, 29, 180-182.

Hadley, J.B. (1950) Geology of the Bradford-Thetford area, Orange County, Vermont. Vermont Geological Survey Bulletin, 1, 31 p.

Heinrich, W., Andrehs, G., and Franz, G. (1997) Monazite-xenotime miscibility gap thermometry. I. An empirical calibration. Journal of Metamorphic Geology, 15, 3-16.

Hickmott, D.D., and Shimizu, N. (1990) Trace element zoning in garnet from the Kwoiek Area, British Columbia: disequilibrium partitioning during garnet growth? Contributions to Mineralogy and Petrology, 104, 619-630.

Hollister, L.S. (1966) Garnet zoning: an interpretation based on the Rayleigh fractionation model. Science, 154, 1647-1651.

Jaffe, H.W. (1951) The role of yttrium and other minor elements in the garnet group. American Mineralogist, 36, 133-155.

Jarosewich, E. and Boatner, L.A. (1991) Rare-earth element reference samples for electron microprobe analysis. Geostandards Newsletter, 15, 397-399.

Kingery, W.D. (1984) Segregation phenomena at surfaces and at grain boundaries in oxides and carbides. Solid State Ionics, 12, 299-307.

Kohn, M.J., Orange, D.L., Spear, F.S., Rumble, D. III, and Harrison, T.M. (1992) Pressure, temperature, and structural evolution of west-central New Hampshire: Hot thrusts over cold basement. Journal of Petrology, 33, 521-556.

Kohn, M.J., Spear, F.S., and Valley, J.W. (1997) Dehydration-melting and fluid recycling during metamorphism: Rangeley formation, New Hampshire, USA. Journal of Petrology, 38, 1255-1277.

Kretz, R. (1983) Symbols for rock-forming minerals. American Mineralogist, 68, 277-279.

Lanzirotti, A. (1995) Yttrium zoning in metamorphic garnets. Geochimica et Cosmochimica Acta, 59, 4105-4110.

Li, C.-W., and Kingery, W.D. (1984) Solute segregation at grain boundaries in polycrystalline Al_2O_3. In: Structure and Properties of MgO and Al_2O_3 ceramics. American Ceramic Society, 368-378.

Menard, T. (1991) Metamorphism of calcic pelitic schists, Strafford Dome, Vermont. Ph. D. Thesis, Rensselaer Polytechnic Institute, 295 p.

Menard, T, and Spear, F.S. (1993) Metamorphism of calcic pelitic schists, Strafford Dome, Vermont: compositional zoning and reaction history. Journal of Petrology, 34, 977-1005.

Menard, T., and Spear, F.S. (1994) Metamorphic P-T paths from calcic pelitic schists from the Strafford Dome, Vermont, USA. Journal of Metamorphic Geology, 12, 811-826.

Pyle, J.M., and Spear, F.S. (1999a) An empirical garnet (YAG)-xenotime thermometer. Contributions to Mineralogy and Petrology, in press.

Pyle, J.M., and Spear, F.S. (1999b) Accessory-mineral and reaction-history controls on pelitic trace-element partitioning: a combined EMP and LA-ICP-MS study (abstract) Eos, Transactions, American Geophysical Union, 80, S356.

Rasband, W. (1997) NIH Image. http://rsb.info.nih.gov/nih-image/.

Reid, M.R. (1990) Ionprobe investigation of rare earth element distributions and partial melting of metasedimentary granulites. In: Vielzeuf, D., and Vidal, P. (eds) Granulites and Crustal Evolution. Kluwer Academic Publishers, Netherlands, pp. 507-522.

Robinson, P., Thompson, P.J., Elbert, D.C. (1991) The nappe theory in the Connecticut Valley region: thirty-five years since Jim Thompson's first proposal. American Mineralogist, 76, 689-712.

Rolph, A.L. (1982) Structure and stratigraphy around the Elizabeth mine, Vermont. M.S. Thesis, University of Cincinnati, 228 p.

Spear, F.S. (1992) Inverted metamorphism, P-T paths, and the cooling history of west-central New Hampshire: implications for the tectonic evolution of central New England. In: Robinson P., and Brady J.B. (eds) Guidebook for Fieldtrips in the Connecticut Valley Region of Massachusetts and the Adjacent States (vol 2). Department of Geology and Geography, University of Massachusetts, Amherst, pp. 446-466.

Spear, F.S. and Florence, F.P. (1992) Thermobarometry in Granulites: pitfalls and new approaches. Precambrian Research, 55, 209-241.

Spear, F.S. and Harrison, T.M. (1989) Geochronologic studies in central New England I: evidence for pre-Acadian metamorphism in eastern Vermont. Geology, 17, 181-184.

Spear, F.S, Hickmott, D.D, and Selverstone, J. (1990) Metamorphic consequences of thrust emplacement, Fall Mountain, New Hampshire. Geological Society of America Bulletin, 102, 1344-1360.

Spear, F.S., Kohn, M.J., Florence, F.P., and Menard, T. (1991) A model for garnet and plagioclase growth in pelitic schists: implications for thermobarometry and P-T path determinations. Journal of Metamorphic Geology, 8, 683-696.

Spear, F.S, Kohn, M.J, and Paetzold, S. (1995) Petrology of the regional sillimanite zone, west-central New Hampshire, U.S.A., with implications for the development of inverted isograds. American Mineralogist, 80, 361-376.

Spear, F.S. and Kohn, M.J. (1996) Trace element zoning in garnet as a monitor of crustal melting. Geology, 24, 1099-1102.

Spear, F.S, Kohn, M.J., and Cheney, J.T. (1999) P-T paths from anatectic pelites. Contributions to Mineralogy and Petrology, 134, 17-32.

Spear, F.S., and Parrish, R.R. (1996) Petrology and cooling rates of the Valhalla Complex, British Columbia, Canada. Journal of Petrology, 37, 733-763.

Stowell, H.H., Menard, T., and Ridgway, C.K. (1996) Ca-metasomatism and chemical zonation of garnet in contact-metamorphic aureoles, Juneau Gold Belt, southeastern Alaska. The Canadian Mineralogist, 34, 1195-1209.

Thompson, J.B. Jr, Robinson, P., Clifford, T.N., and Trask, N.J. (1968) Nappes and gneiss domes in west-central New England. In: Zen, E-an, White, W.S., Hadley, J.B., and Thompson, J.B. Jr. (eds) Studies of Appalachian Geology, Northern and Maritime. John Wiley and Sons, New York , 319-327.

Wark, D.A., and Miller, C.L. (1993) Accessory mineral behavior during differentiation of a granite suite: monazite, xenotime and zircon in the Sweetwater Wash pluton, southeastern California, U.S.A. Chemical Geology, 110, 49-67.

Watson, E.B. (1996) Surface enrichment and trace-element uptake during crystal growth. Geochimica et Cosmochimica Acta, 60, 5013-5020.

Welch, P.W. and Tracy, R.J. (1998) Major and trace element zoning in a complex polymetamorphic garnet, Gassetts, Vermont (abstract). Eos, Transactions, American Geophysical Union, 79 (17), Spring Meeting Supplement, S381.

Wopenka, B., Jolliff, B.L., Zinner, E., and Kremser, D.T. (1996) Trace element zoning and incipient metamictization in a lunar zircon: application of three microprobe techniques. American Mineralogist, 81, 902-912.

Yang, P., Rivers, T., and Jackson, S. (1999) Crystal-chemical and thermal controls on trace-element partitioning between coexisting garnet and biotite in metamorphic rocks from western Labrador. The Canadian Mineralogist, 37, 443-468.

Yoder, H.S. and Keith, M.L. (1951) Complete substitution of aluminum for silicon: the system $3MnO \cdot Al_2O3 \cdot 3SiO_2 - 3Y_2O_3 \cdot 5Al_2O_3$. American Mineralogist, 36, 519-533.

Table 1. Sample grade and accessory mineral assemblage

sample	grade	Mon	Ap	Zrn	Ilm	Fe-sulfide	Xen	other
92-53	Grt	X	X	X		X	r	Rt
BF-15A	Grt	X	X	X	X		m	
PUT-92C2	Grt	X		X	X	X		
93-19A	Grt	X	X	X	X	X	m,r	Ccp, Sp, Rt
TM-458A	Grt		X	X	X			Tur, Rt, Ep
TM-549	Grt	X	X	X	X		i	Tur, Rt, Ank
TM-534	Grt		X	X	X			Ep, Gr
TM-747	Grt		X	X	X	X		Ep,Tur,Gr,
BF-17A	St	X	X	X		X	i	Gr, Rt
BF-17D	St	X	X	X		X		Rt
BF-18C	St	X	X	X	X	X	r?	
BF-38B1B	St	X	X	X	X		i	
BF-52A	St	X	X	X	X	X	r	
BF-57B	St	X		X	X	X	r?	Sp
BF-58B	St	X		X	X			
BF-64	St	X	X	X	X	X	r	Rt
TM-445	St	X	X	X	X		m	Ep, Ttn, Gr, Mt
TM-637	St-Ky	X	X	X	X			Ep,Gr, Tur
BF-92B	Sil	X		X	X		i	
89-9	Sil	X	X	X	X	X	i	Rt, Gr
89-22	Sil	X	X	X	X		i	
BF-78	Sil	X	X	X	X	X	i	
BF-9H	Mig	X	X	X	X	X	i,r	Rt
BF-14P	Mig	X	X	X	X		i,r	Spl
K92-12D	Mig	X	X	X	X			
LM-1A2	Mig	X	X	X	X	X	i	Rt, Ccp
LM-1E	Mig	X		X	X	X	i	Rt
V6A	Mig	X		X	X			Rt
V7C	Mig	X		X	X	X		Rt

X: mineral identified in sample
i: xenotime present as inclusion in garnet
m: xenotime present as matrix phase
r: xenotime present in reaction zone in or around garnet
?: indicates tentative identification only
Mineral abbreviations after Kretz (1983)

Table 2. Garnet trace-element analyses (values in ppm)

	89-22B-A c (5)	89-22B-A r (5)	89-22B-C c (5)	89-22B-C r (5)	89-22B-B c (5)	89-22B-B r (4)
Na	466 (104)	390 (166)	315 (116)	220 (127)	289 (39)	306 (67)
Ti	117 (12)	<100	<100	<100	<100	<100
Sc	201 (42)	<100	129 (29)	<100	113 (13)	<100
P	<100	<100	<100	<100	<100	<100
Y	241 (53)	619 (81)	216 (137)	445 (99)	182 (94)	597 (113)
Cr	<100	<100	<100	<100	<100	<100

	89-9A-A c (2)	89-9A-A r (5)	89-9A-B c (4)	89-9A-B r (5)	93-19A-B c (5)	93-19A-B r (5)
Na	202 (49)	137 (89)	195 (125)	<100	118 (17)	<100
Ti	280 (187)	<100	<100	211 (101)	136 (33)	126 (30)
Sc	150 (51)	153 (25)	157 (23)	159 (19)	<100	<100
P	<100	<100	<100	<100	<100	<100
Y	234 (15)	207 (47)	547 (92)	209 (71)	2149 (57)	1509 (89)
Cr	<100	<100	<100	113 (53)	<100	<100

	93-19A-C c (1)	93-19A-C o (5)	93-19A-C r (5)	BF-14P-A c (5)	BF-14P-A a (5)	BF-14P-A r (5)
Na	<100	116 (30)	115 (27)	169 (63)	110 (23)	245 (128)
Ti	<100	117 (23)	<100	172 (31)	200 (18)	<100
Sc	<100	<100	<100	544 (51)	992 (28)	179 (54)
P	<100	<100	<100	137 (31)	105 (39)	<100
Y	1732	2082 (38)	1407 (189)	1059 (26)	1245 (21)	154 (13)
Cr	<100	<100	<100	523 (43)	1188 (32)	115 (93)

	BF-17A-A c (5)	BF-17A-A o (5)	BF-17A-A r (5)	BF-17A-B c (5)	BF-17A-B r (5)	BF-17D-A c (5)
Na	465 (67)	419 (45)	<100	416 (20)	<100	302 (37)
Ti	495 (153)	428 (59)	405 (52)	584 (182)	468 (59)	229 (31)
Sc	<100	<100	220 (31)	<100	173 (11)	<100
P	105 (7)	<100	138 (14)	<100	125 (24)	<100
Y	4341 (230)	5346 (250)	<100	5061 (163)	<100	2287 (67)
Cr	<100	<100	<100	<100	<100	<100

	BF-17D-A o (5)	BF-17D-A r (5)	BF-17D-B c (5)	BF-17D-B r (5)	BF-18C-A c (5)	BF-18C-A r (5)
Na	269 (77)	126 (95)	207 (31)	<100	300 (45)	110 (47)
Ti	209 (88)	138 (18)	147 (31)	<100	137 (23)	110 (24)
Sc	<100	139 (10)	<100	137 (19)	<100	123 (13)
P	101 (24)	<100	107 (21)	110 (17)	<100	124 (6)
Y	1978 (253)	133 (43)	1669 (168)	<100	2124 (80)	<100
Cr	<100	<100	<100	<100	<100	<100

Table 2. Garnet trace-element analyses (cont.)

	BF-38B-A c (5)	BF-38B-A a (5)	BF-38B-A r (5)	BF-38B-B c (5)	BF-38B-B o (5)	BF-38B-B a (5)
Na	731 (159)	289 (85)	173 (34)	384 (368)	164 (32)	192 (34)
Ti	206 (184)	175 (49)	144 (25)	453 (123)	283 (25)	<100
Sc	<100	<100	108 (20)	183 (18)	153 (10)	<100
P	<100	<100	<100	110 (25)	100 (44)	<100
Y	2783 (198)	1193 (97)	241 (59)	1217 (45)	659 (51)	1374 (108)
Cr	<100	<100	<100	114 (39)	114 (61)	<100

	BF-38B-B r (5)	BF-52A-A c (5)	BF-52A-A a (5)	BF-52A-A r (5)	BF-52A-B c (5)	BF-52A-B r (5)
Na	168 (58)	141 (64)	159 (21)	<100	153 (35)	<100
Ti	<100	569 (24)	214 (53)	179 (37)	188 (50)	160 (24)
Sc	118 (11)	246 (58)	<100	112 (21)	<100	<100
P	121 (14)	173 (8)	<100	<100	<100	<100
Y	184 (54)	234 (148)	1203 (61)	<100	1143 (155)	<100
Cr	<100	<100	<100	<100	<100	<100

	BF-52A-C c (5)	BF-52A-C r (5)	BF-57B-A c (5)	BF-57B-A o (5)	BF-57B-A r (4)	BF-57B-B c (5)
Na	193 (57)	<100	267 (29)	186 (35)	<100	180 (27)
Ti	256 (27)	171 (28)	217 (28)	<100	171 (41)	<100
Sc	<100	112 (28)	<100	<100	102 (13)	<100
P	108 (27)	100 (15)	<100	<100	123 (21)	<100
Y	1217 (84)	<100	2468 (121)	1442 (155)	176 (49)	1390 (40)
Cr	<100	<100	<100	<100	<100	<100

	BF-57B-B r (5)	BF-58B-A c (4)	BF-58B-A r (5)	BF-58B-B c (5)	BF-58B-B r (5)	BF-64A-A c (5)
Na	<100	282 (29)	<100	260 (22)	<100	256 (20)
Ti	143 (52)	239 (32)	174 (42)	204 (22)	172 (24)	302 (32)
Sc	109 (27)	<100	150 (27)	<100	<100	<100
P	110 (29)	<100	104 (26)	<100	<100	108 (19)
Y	<100	2440 (133)	<100	2174 (161)	<100	3047 (95)
Cr	<100	<100	<100	<100	<100	<100

	BF-64A-A r (5)	BF-64A-B c (5)	BF-64A-C c (5)	BF-78-A c (5)	BF-78-A r (5)	BF-78-E c (5)
Na	295 (283)	1223 (431)	308 (69)	<100	<100	<100
Ti	244 (19)	332 (207)	235 (41)	<100	<100	<100
Sc	121 (31)	<100	<100	125 (29)	214 (48)	162 (14)
P	100 (16)	<100	112 (7)	<100	230 (19)	155 (19)
Y	112 (42)	2356 (187)	2557 (169)	271 (80)	123 (33)	389 (29)
Cr	<100	<100	<100	<100	<100	<100

Table 2. Garnet trace-element analyses (cont.)

	BF-78-E a (5)	BF-78-E r (5)	LM-1A2-A c (5)	LM-1A2-A r (5)	LM-1A2-B c (5)	LM-1A2-B r (5)
Na	<100	<100	210 (34)	<100	217 (82)	199 (80)
Ti	106 (39)	122 (51)	<100	116 (14)	<100	<100
Sc	229 (31)	175 (13)	112 (25)	232 (28)	118 (35)	216 (60)
P	231 (25)	<100	<100	178 (15)	<100	275 (39))
Y	388 (46)	271 (43)	1899 (62)	106 (66)	1351 (58)	<100
Cr	163 (30)	<100	<100	141 (44)	<100	101 (42)

	LM-1A2-C c (5)	LM-1A2-C r (5)	LM-1E-A c (5)	LM-1E-A r (5)	PUT-92C2A c (5)	PUT-92C2A o (4)
Na	<100	<100	201 (10)	141 (43)	232 (101)	141 (1)
Ti	<100	<100	<100	<100	400 (68)	201 (49)
Sc	108 (63)	283 (32)	104 (21)	126 (22)	181 (27)	<100
P	<100	<100	123 (18)	105 (107)	125 (59)	<100
Y	203 (99)	109 (55)	1585 (127)	148 (52)	263 (46)	521 (40)
Cr	<100	172 (25)	<100	109 (62)	<100	<100

	PUT-92C2A er (5)	PUT-92C2C c (1) (Grt A)	PUT-92C2C o (5) (Grt A)	PUT-92C2C r (3) (Grt A)	PUT-92C2C o (5) (Grt B)	PUT-92C2C er (5)(Grt B)
Na	225 (44)	206	150 (59)	170 (25)	143 (78)	239 (81)
Ti	<100	376	504 (41)	104 (15)	190 (36)	<100
Sc	<100	<100	209 (26)	<100	<100	<100
P	103 (36)	149	186 (106)	112 (15)	147 (96)	122 (62)
Y	1029 (172)	1902	233 (76)	570 (108)	523 (65)	1253 (146)
Cr	<100	101	<100	<100	<100	<100

	TM-445-A c (3)	TM-445-A o#1 (5)	TM-445-A o#2 (4)	TM-445-A a (5)	TM-445-A r (5)	TM-445-B c (5)
Na	268 (66)	221 (29)	144 (48)	351 (24)	152 (5)	194 (48)
Ti	972 (72)	911 (86)	516 (40)	<100	<100	912 (206)
Sc	216 (47)	321 (25)	152 (24)	<100	<100	288 (50)
P	180 (9)	171 (25)	195 (10)	<100	<100	121 (22)
Y	292 (29)	357 (45)	246 (56)	2475 (59)	629 (76)	337 (57)
Cr	186 (20)	<100	108 (46)	<100	159 (51)	133 (28)

	TM-445-B o#1 (5)	TM-445-B a (5)	TM-445-B o#2 (5)	TM-445-B r (5)	TM-458-A c (4)	TM-458-A o#1 (5)
Na	134 (19)	391 (26)	260 (57)	145 (26)	186 (36)	205 (24)
Ti	587 (45)	<100	106 (91)	<100	981 (96)	821 (99)
Sc	136 (25)	<100	<100	<100	<100	101 (21)
P	106 (24)	<100	<100	<100	122 (9)	118 (14)
Y	185 (24)	2479 (74)	1605 (197)	773 (51)	<100	<100
Cr	<100	<100	123 (30)	154 (50)	<100	182 (64)

Table 2. Garnet trace-element analyses (cont.)

	TM-458-A o#2 (5)	TM-458-A r (5)	TM-549-A c (5)	TM-549-A o (4)	TM-549-B c (5)	TM-549-B o (4)
Na	453 (284)	208 (23)	543 (84)	106 (42)	521 (77)	142 (27)
Ti	750 (133)	430 (77)	367 (34)	572 (285)	383 (24)	384 (20)
Sc	<100	<100	<100	<100	<100	103 (35)
P	132 (14)	125 (14)	112 (20)	163 (96)	129 (18)	166 (26)
Y	<100	310 (42)	4030 (648)	517 (448)	3783 (322)	732 (92)
Cr	251 (70)	448 (90)	185 (36)	163 (109)	123 (21)	145 (41)

	TM-637-A c (5)	TM-637-A a (5)	TM-637-A o (5)	TM-637-A r (3)	TM-637-A er (4)	TM-637-B c (5)
Na	172 (23)	201 (32)	113 (29)	150 (18)	165 (12)	246 (17)
Ti	787 (38)	451 (66)	577 (58)	430 (163)	109 (50)	535 (57)
Sc	334 (35)	172 (33)	<100	108 (7)	<100	234 (22)
P	139 (25)	115 (22)	141 (16)	108 (11)	<100	135 (20)
Y	<100	386 (83)	<100	172 (6)	584 (46)	394 (50)
Cr	130 (32)	<100	<100	134 (12)	178 (40)	102 (23)

	TM-637-B o (4)	TM-637-B r#1 (4)	TM-637-B r#2 (1)	TM-747-A c (5)	TM-747-A o#1 (5)	TM-747-A o#2 (5)
Na	145 (18)	123 (36)	<100	141 (24)	<100	<100
Ti	562 (23)	110 (13)	169	691 (22)	470 (38)	328 (36)
Sc	142 (38)	<100	117	316 (63)	<100	<100
P	131 (2)	<100	<100	128 (7)	129 (19)	118 (18)
Y	<100	425 (37)	536	415 (84)	<100	<100
Cr	163 (40)	170 (22)	328	<100	<100	116 (39)

	V6A–A c (5)	V6A-A o (5)	V6A-A r (5)	V7C-A c (5)	V7C-A r (5)
Na	<100	<100	<100	135 (28)	<100
Ti	132 (16)	133 (17)	147 (28)	<100	<100
Sc	172 (33)	146 (31)	<100	236 (12)	116 (34)
P	140 (22)	119 (22)	162 (16)	193 (20)	284 (30)
Y	340 (43)	<100	<100	599 (57)	<100
Cr	<100	158 (26)	103 (28)	<100	100 (27)

numbers in parentheses next to concentrations are standard deviations (1σ) of multiple analyses
c: core analysis
a: annulus analysis
o: outboard analysis (either outboard of core, or outboard of annulus if it follows an ‘a’ analysis)
r: rim analysis
er: extreme rim analysis (outer 50 μm of garnet)
number in parentheses adjacent to analysis position indicates number of spot analyses taken for average

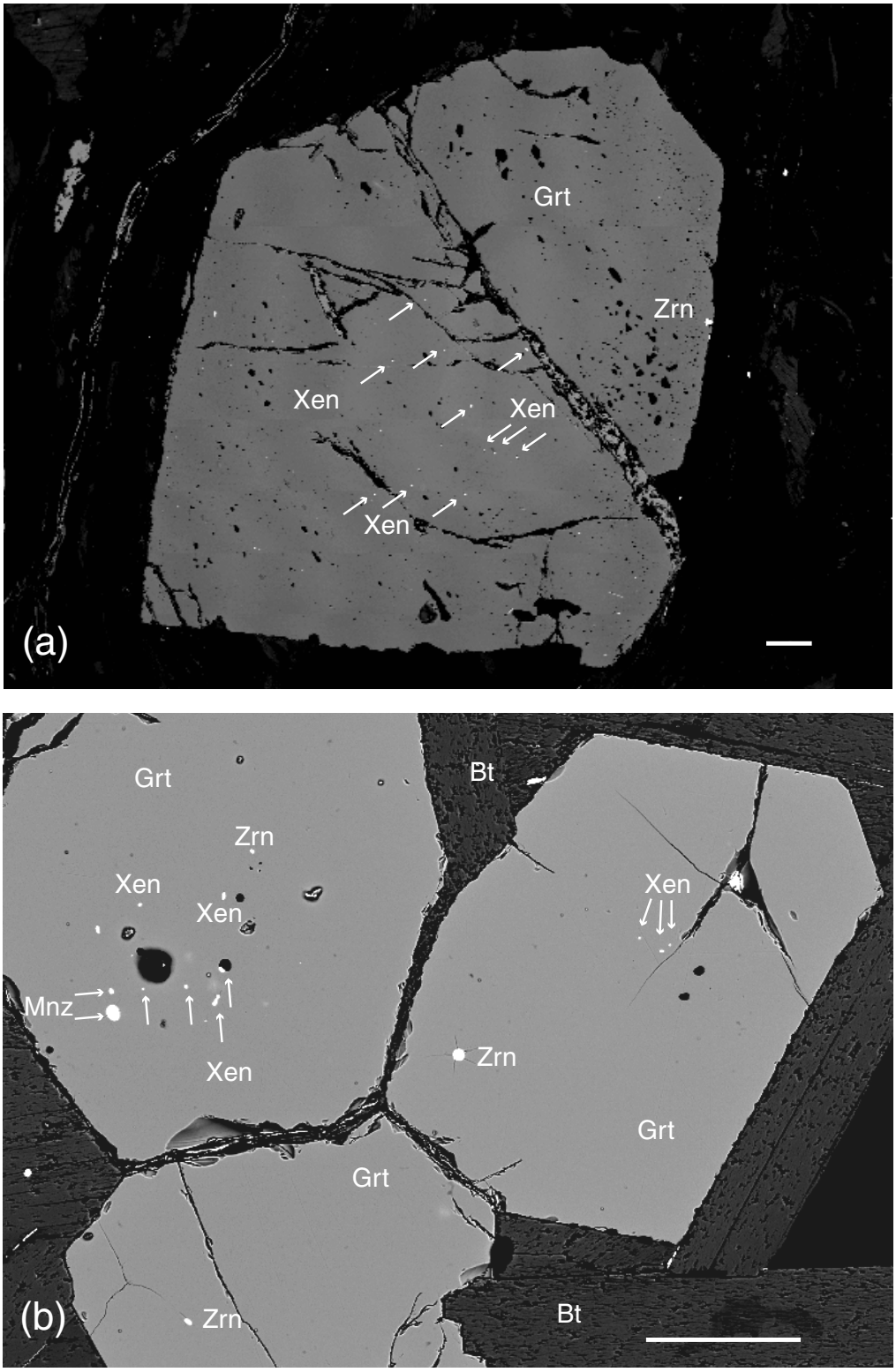

Figure 1. BEIs (BEI = back-scatter electron image) showing xenotime inclusions in garnet cores. (a) BF-17A, garnet B (staurolite zone). (b) BF-78 (sillimanite zone). Grt = garnet, Bt = biotite, Xen = xenotime, Zrn = zircon, Mnz = monazite. Scale bars = 100 μm.

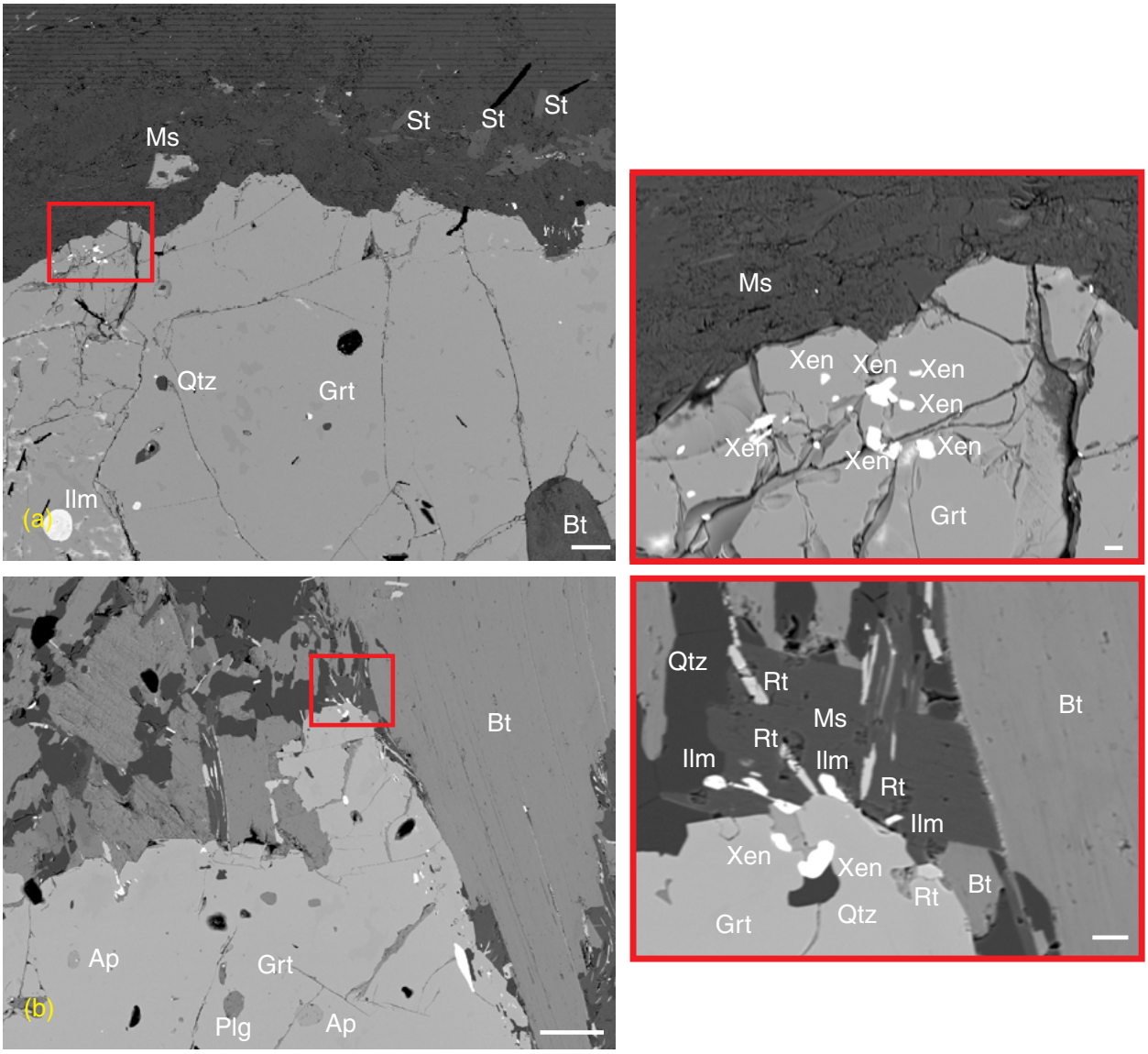

Figure 2. BEIs showing inclusions of xenotime near garnet rims in migmatite zone pelites. (a) Sample BF-14P. Enlargement shows aggregate of xenotime just inside of garnet rim. (b) Sample BF-9H. Enlargement shows aggregates of ilmenite and xenotime near garnet rim. Grt = garnet, Xen = xenotime, Ms = muscovite, Ilm = ilmenite, Rt = rutile, Qtz = quartz, Ap = apatite, St = staurolite, Bt = biotite, Plg = plagioclase. Scale bars = 100 µm in large-scale images, 10 µm in enlargements.

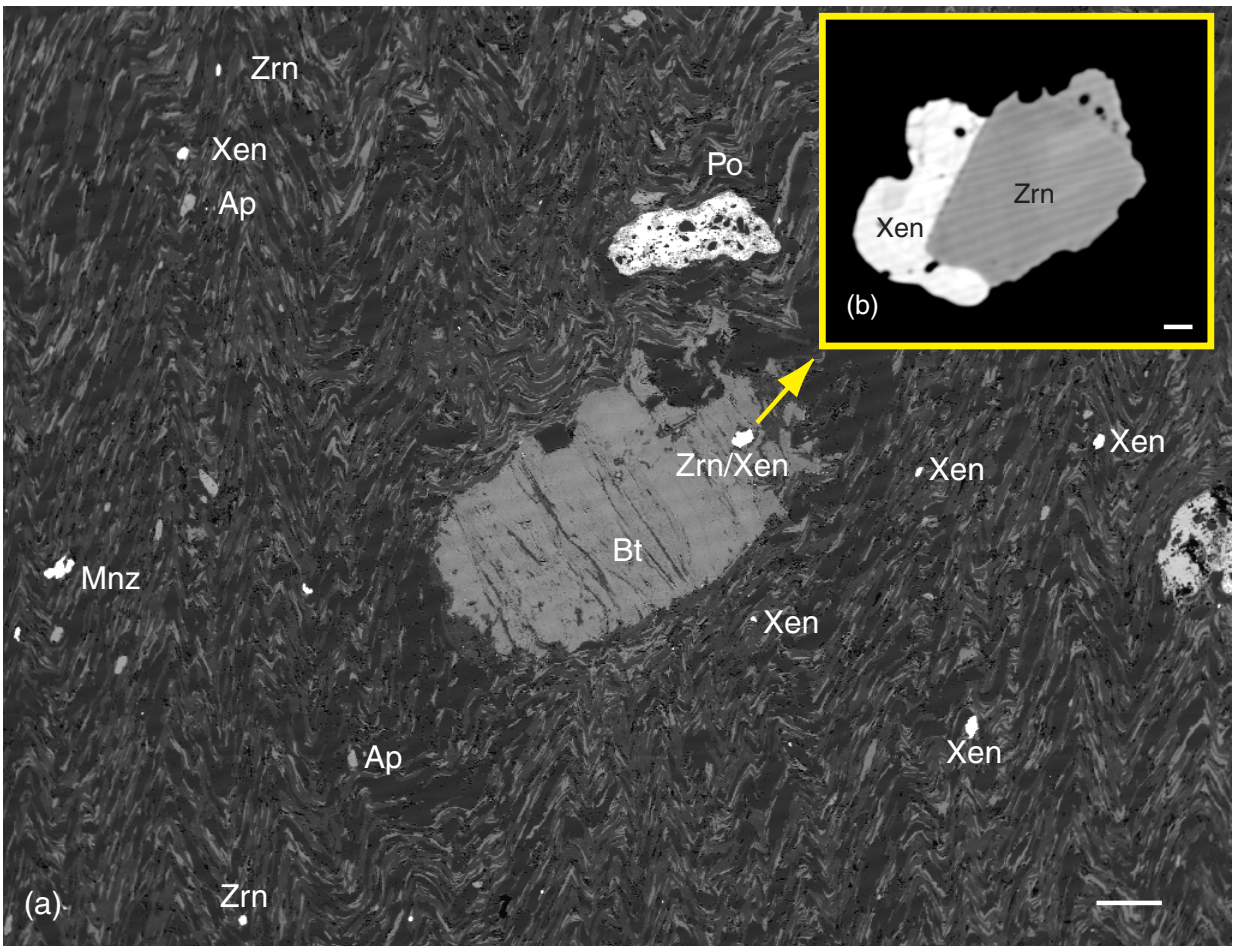

Figure 3. BEI showing xenotime habit in a garnet-zone pelite (sample 93-19A). (a) Low-magnification image (scale bar = 100 µm) showing locations of abundant matrix xenotime. Of the samples examined in this study, only garnet-zone pelites contain abundant matrix xenotime. This sample also contains zircon with xenotime overgrowths and xenotime inclusions in biotite, but no xenotime inclusions in garnet. (b) Higher magnification image (scale bar = 10 µm) of xenotime overgrowth on zircon. Zircon displays internal zoning in BEI image. Ap = apatite, Bt = biotite, Mnz = monazite, Po = pyrrhotite, Xen = xenotime, Zrn = zircon, Zrn/Xen = xenotime overgrowth on zircon. Stripes over Zrn in (b) are an imaging artefact.

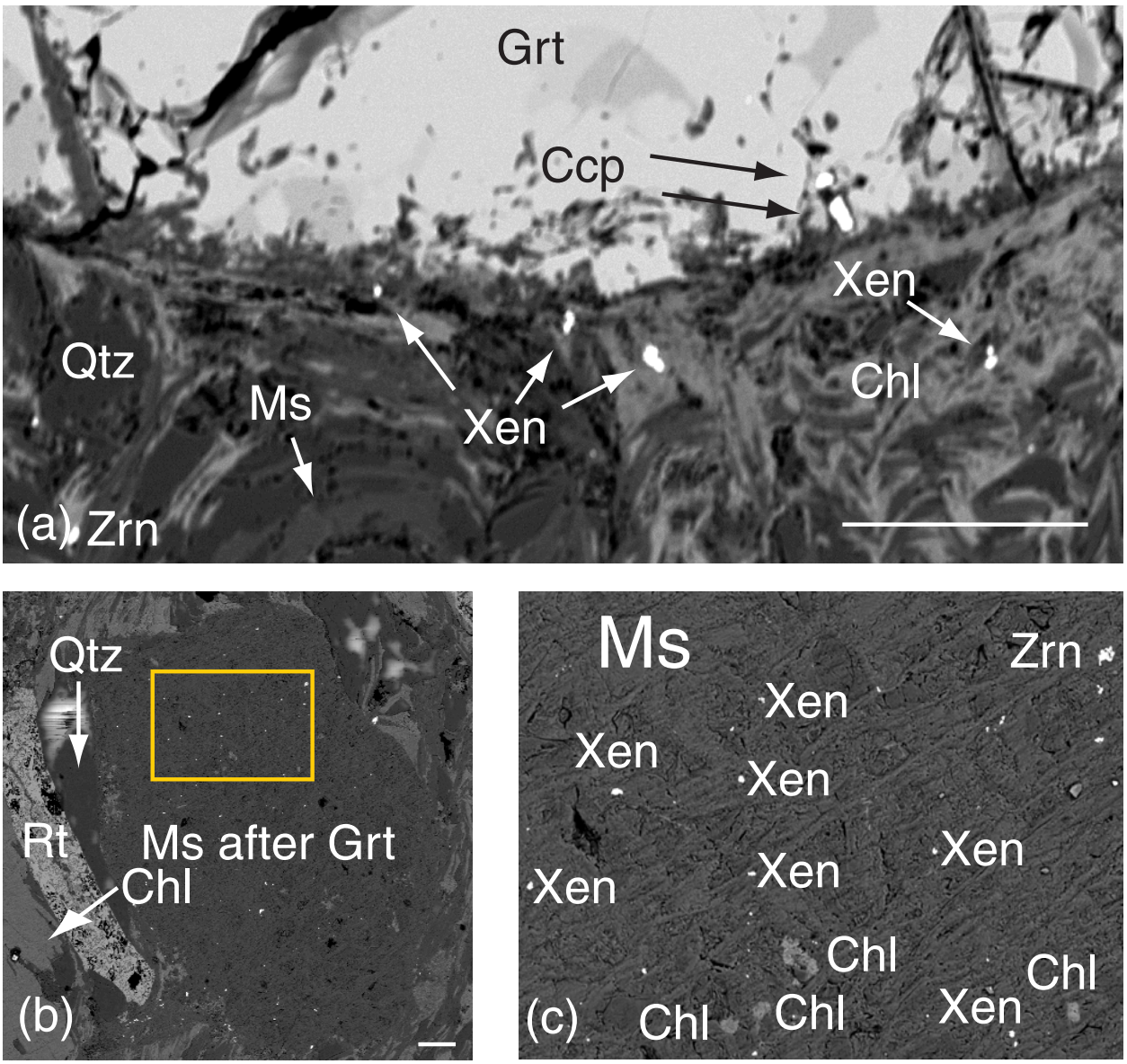

Figure 4. BEIs showing examples of reaction-zone xenotime in garnet-zone samples, 93-19A (a) and 92-53 (b,c). (a) Reaction zone xenotime. Xenotime grains are spatially associated with matrix adjacent to garnet and/or reaction products (biotite, chlorite) rimming garnet (scale bar = 100 μm). Grt = garnet, Chl = chlorite, Xen = xenotime. Ccp = chalcopyrite, Zrn = zircon. In (c) and (d), garnet is pseudomorphed by muscovite (Ms), and pseudomorph contains abundant Xen, with subordinate Chl and Zrn. Scale bar in (b) = 100 μm, and box gives location of enlargement in (c).

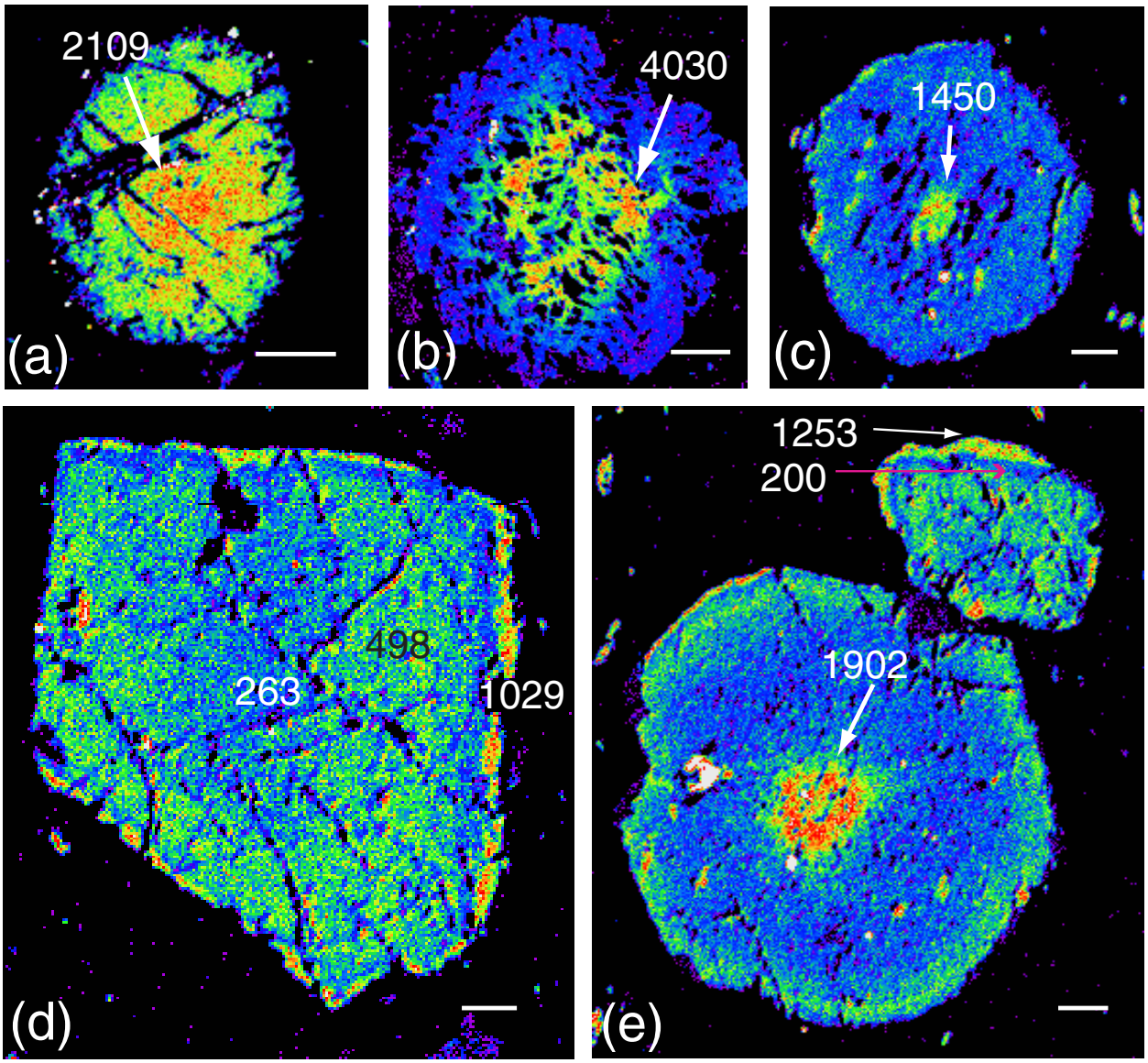

Figure 5. Garnet Y distribution maps, garnet zone samples. (a) 93-19A. (b) TM-549. (c) PUT-92C2 garnet B. (d) PUT-92C2 garnet A. (e) PUT-92C2 garnets C and D. The above images show the variety of core concentrations and zoning patterns seen in low-grade pelitic garnets. Numbers = Y concentrations in ppm. Warm colors indicate higher concentration of Y. All scale bars = 100 μm.

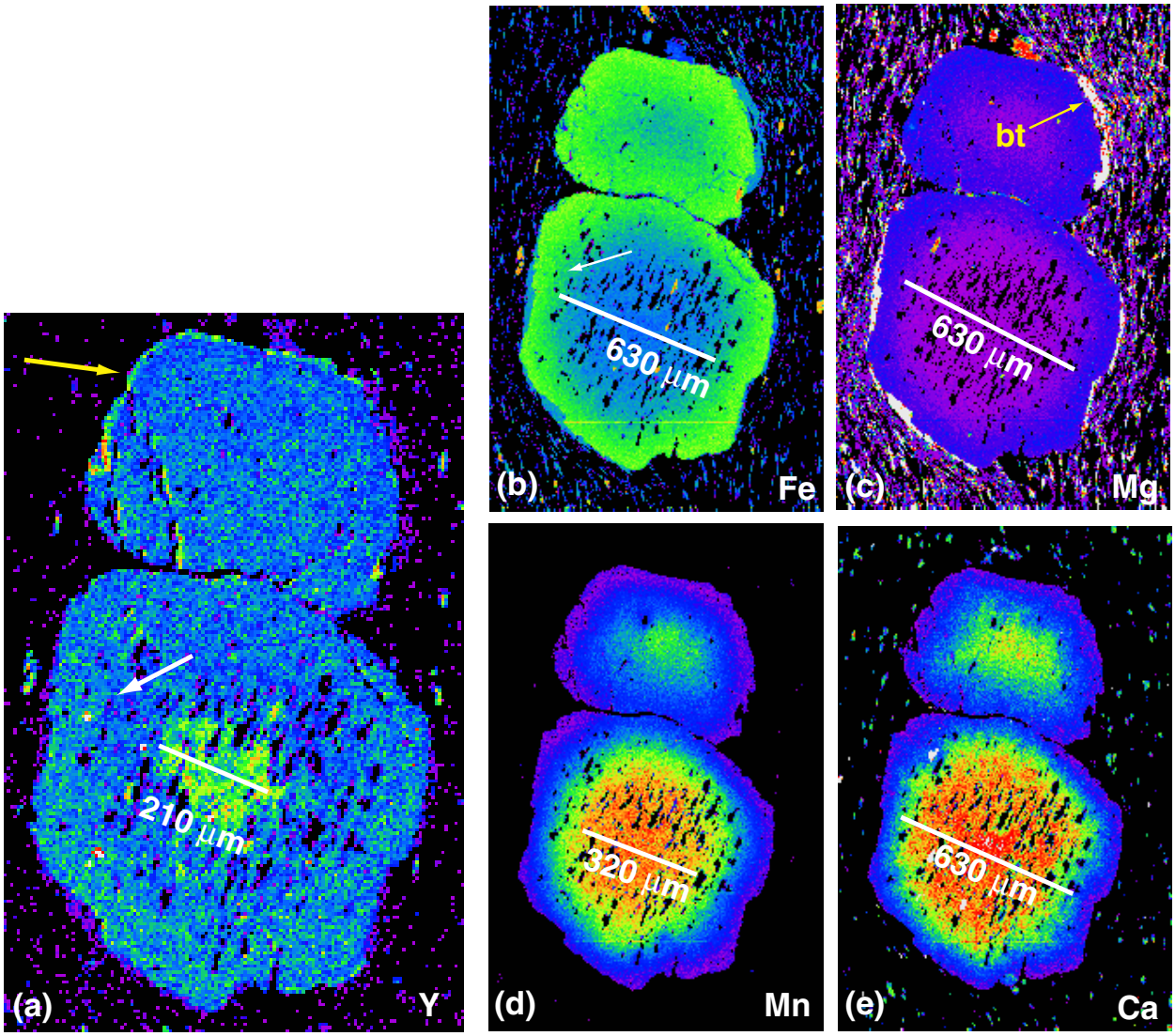

Figure 6. Comparison of Y and major-element zoning in garnet-zone sample PUT-92C2. (a) Y distribution map. (b) Fe. (c) Mg. (d) Mn. (e) Ca. Garnet displays a high-Y core that is significantly smaller (210 µm diameter) than the low Fe and Mg region or high Ca region (630 µm diameter), or the high Mn region (320 µm diameter). A slight increase in yttrium concentration outboard of the core corresponds to an increase in iron concentration (white arrows in (a) and (b), but a noticeable increase in yttrium concentration on the extreme garnet rim (yellow arrow in (a)) is not recorded by other elements. The extreme-rim increase in [Y] is especially noticeable in Fig. 5e, which is a different garnet from the same sample.

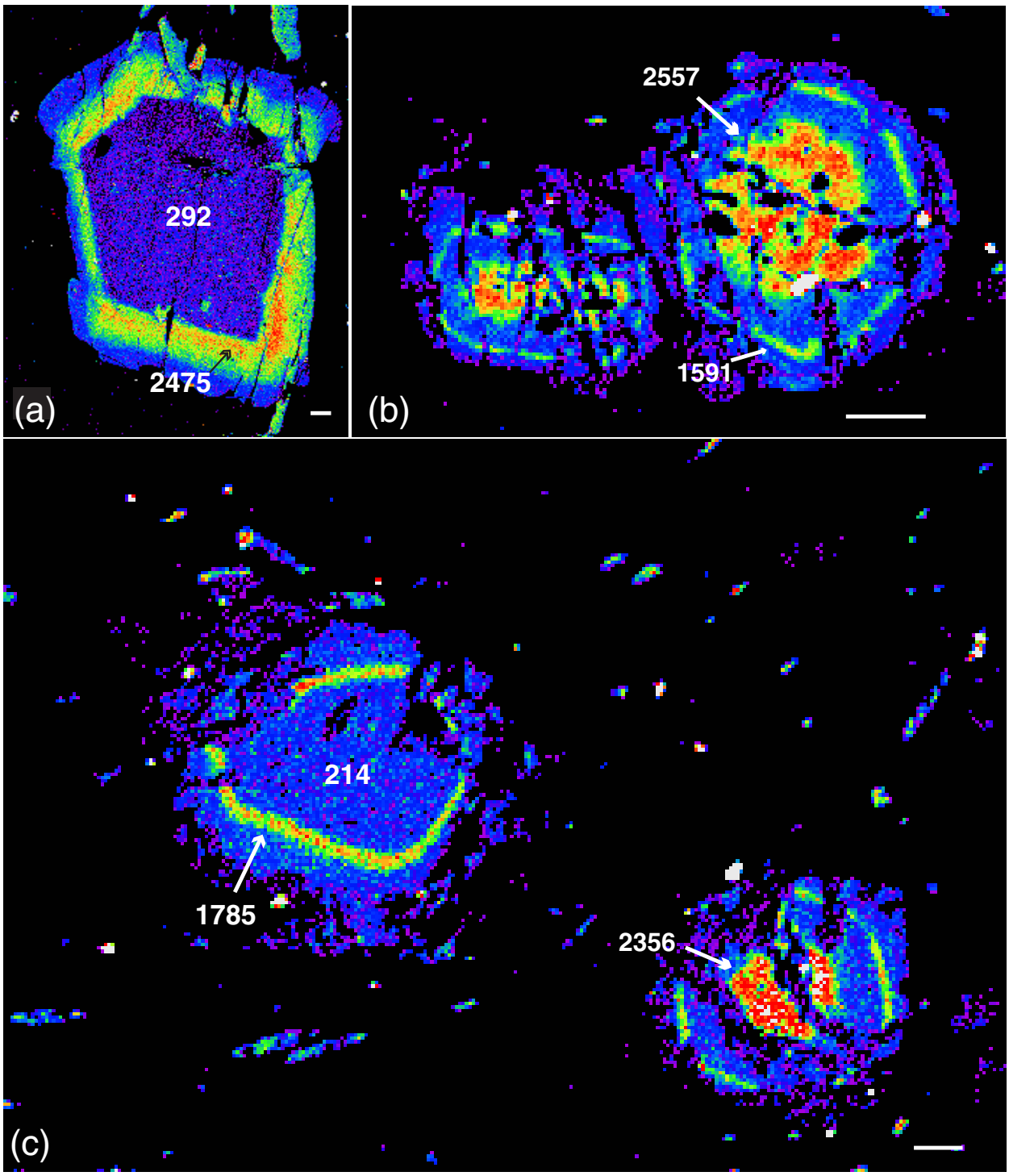

Figure 7. Staurolite zone garnet Y distribution maps displaying high-yttrium annuli. (a) TM-445 garnet A. (b) BF-64 garnets C-A and C-B. (c) BF-64 garnets B-A and B-B. TM-445 contains epidote and titanite as garnet core inclusions, with limited matrix xenotime and monazite. Neither garnet-core inclusion xenotime nor matrix xenotime has been identified in BF-64, but cross-cutting chlorite contains xenotime. Annular widths vary between 20 and 300 μm. All scale bars =100 μm. Numbers = Y concentrations in ppm.

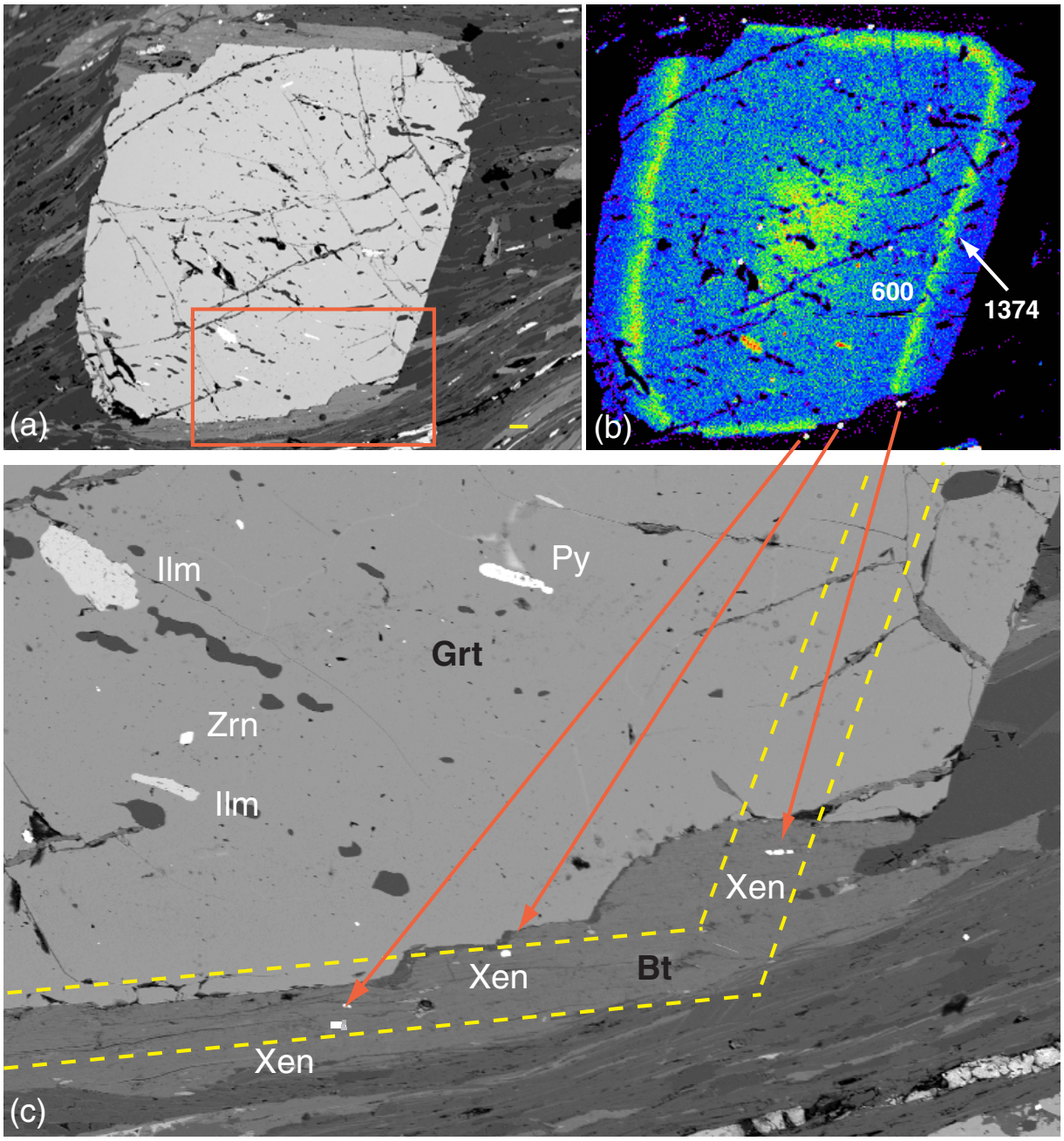

Figure 8. Relationship between yttrium annulus in garnet and reaction-zone xenotime distribution, sample BF-38B1 (staurolite zone). (a) Low magnification (scale bar = 100 μm) BEI of garnet showing rims of biotite. (b) Yttrium distribution map of garnet in (a) showing high-Y annulus truncated by biotite rim and xenotime (three white dots) in biotite on lower garnet rim. (c) Enlargement of image (a); xenotime grains are located in the projected position (yellow dotted lines) of the truncated annulus. Projection assumes lower and right annulus were of equal width prior to garnet consumption. Grt = garnet, Bt = biotite, Ilm = ilmenite, Zrn = zircon, Py = pyrite. Numbers = Y concentrations in ppm.

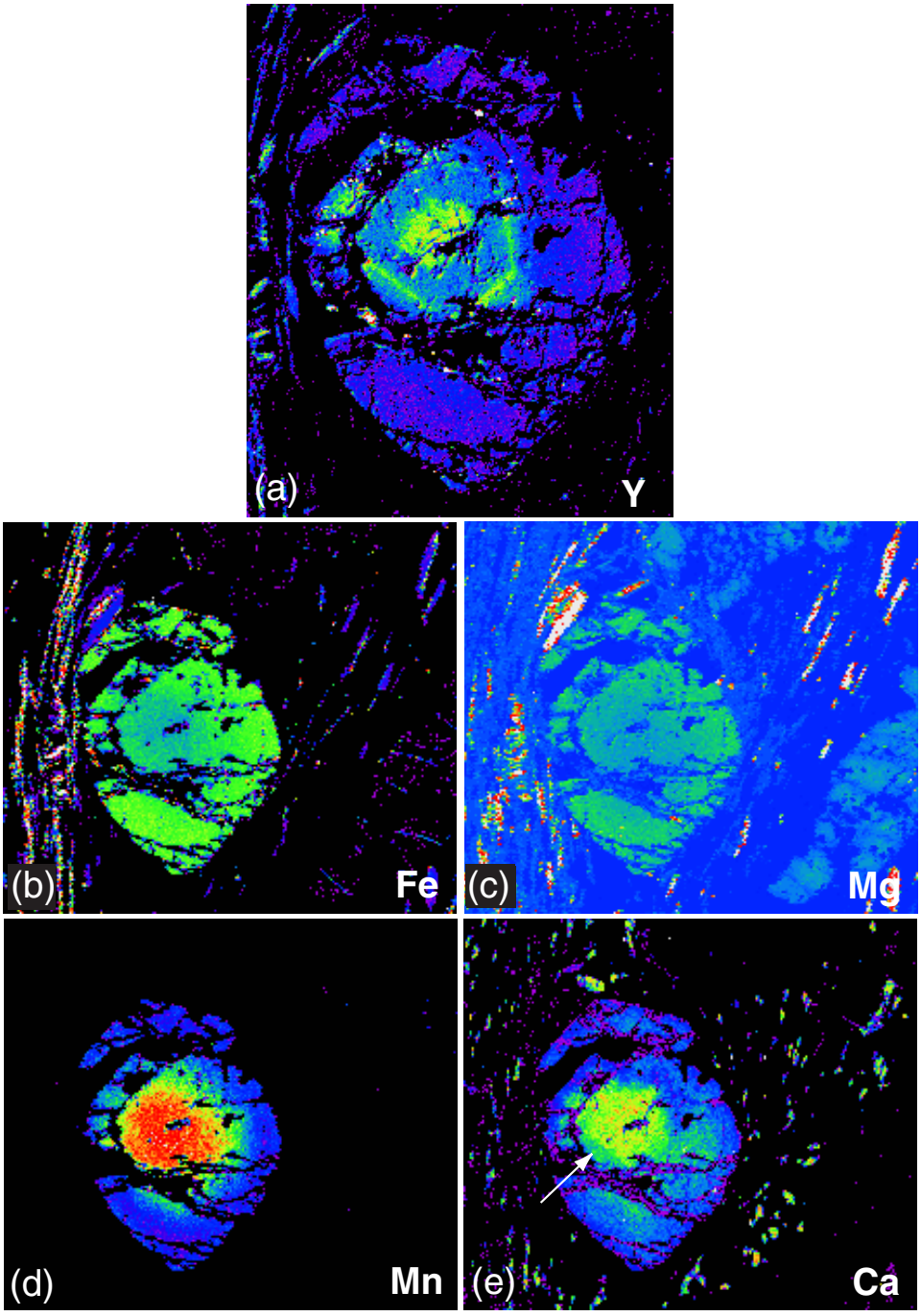

Figure 9. Comparison between yttrium and major-element zoning in garnet, sample BF-87A (staurolite zone): (a) Y; (b) Fe; (c) Mg; (d) Mn; (e) Ca. Garnet crystal is 1.34 mm x 0.9 mm in size. Warm colors indicate higher concentrations of the mapped element. Area of high-yttrium core in (a) does not correspond to any zoning feature in the other maps. The inside of the yttrium annulus corresponds to break in Ca zoning (white arrow), but the moderately high-Ca region right of and below the core does not correspond to any feature in the yttrium map. Low Fe core in (b) corresponds generally, but not exactly, to the hi-Y core in (a), and the Y annulus does not correspond to any feature on the Fe map.

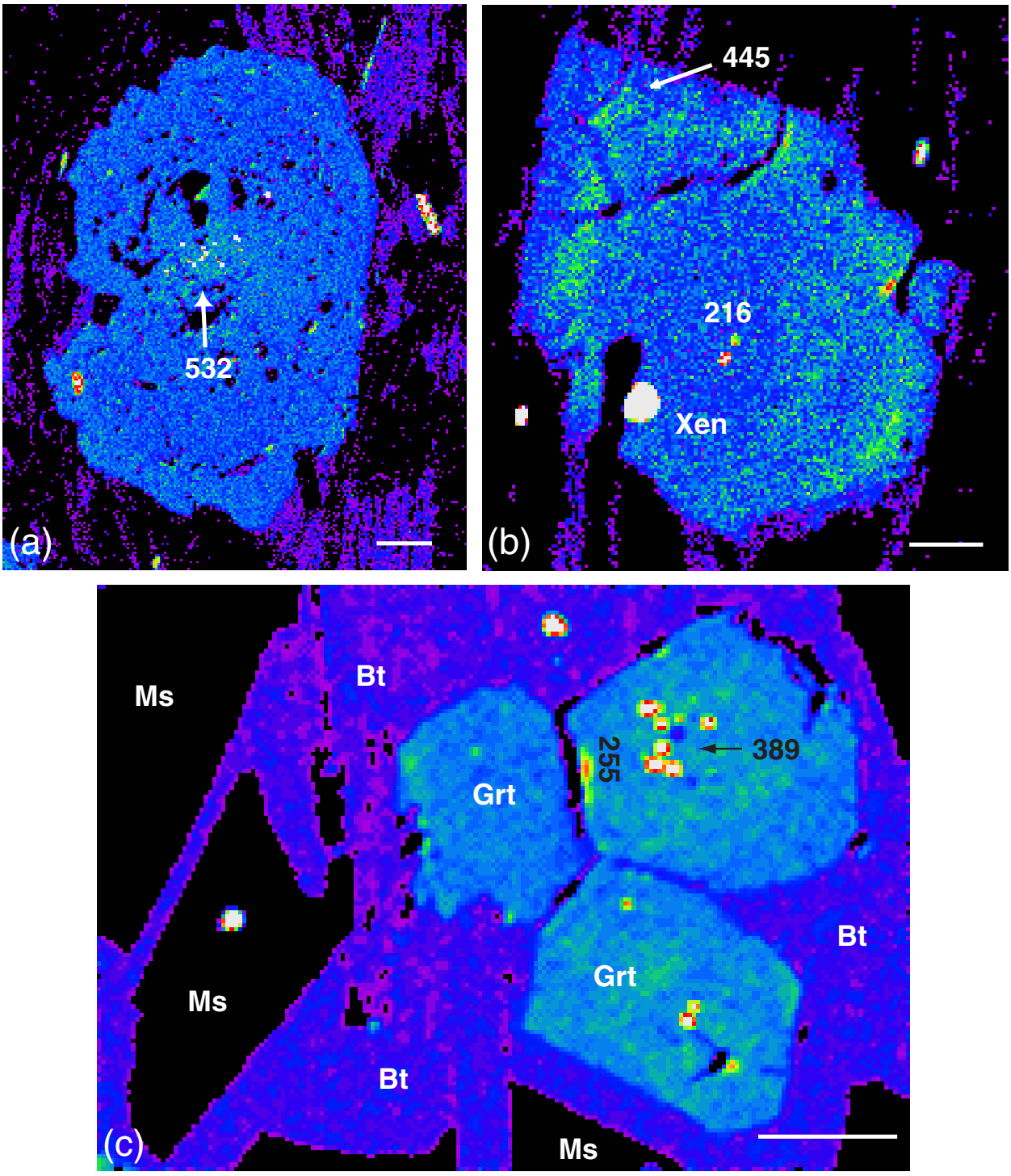

Figure 10. Garnet Y distribution maps, sillimanite-zone samples. (a) 89-9A garnet B. (b) 89-22B garnet C. (c) BF-78 garnet E. Xenotime-bearing samples of sillimanite grade generally contain garnet with less Y than garnets in xenotime-bearing samples of lower grade. All three samples contain xenotime as garnet inclusions. Xen = xenotime, Ms = muscovite, Bt = biotite, Grt = garnet. All scale bars = 100 µm. Numbers = Y concentrations in ppm.

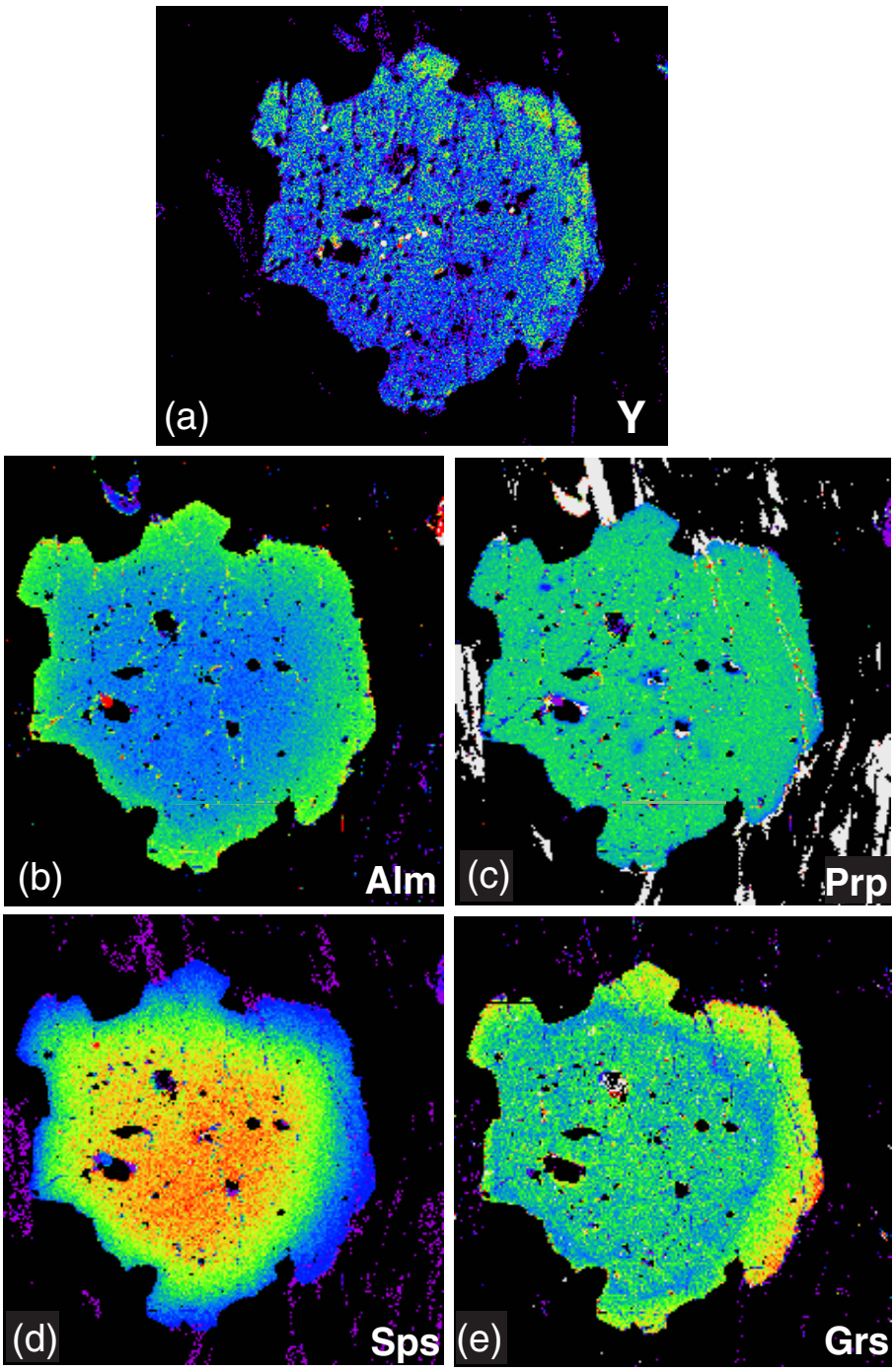

Figure 11. Comparison between yttrium and major-element zoning in garnet, sample 89-22B (sillimanite zone): (a) Y; (b) Alm; (b) Prp; (d) Sps; (e) Grs. Diameter of garnet crystal is 1.1 mm. Warm colors indicate higher concentrations of the mapped element or component. Y increases from core to rim and displays truncation of rim zoning in the lower left side of the garnet. Similar truncation is seen in Alm, Pyp and Sps. Xenotime is present as inclusions and in the matrix. Spear et al. (1995) interpreted these garnets to have grown during near isobaric cooling, which is consistent with the observed rimward increase in $[Y]_{Grt}$ in xenotime bearing pelites (Pyle and Spear, 1999a). Alm: almandine, Prp: pyrope, Sps: spessartine, Grs: grossular.

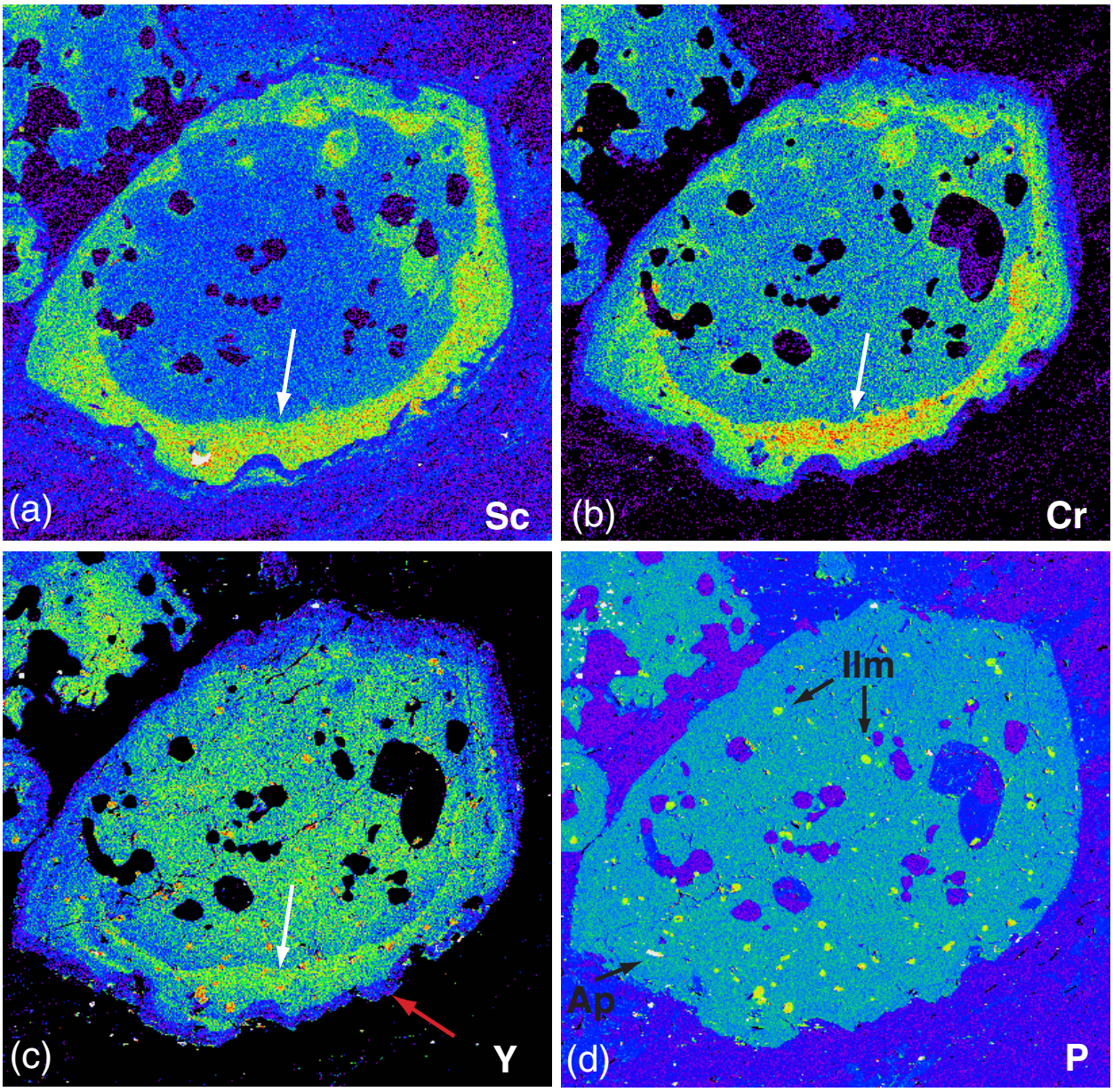

Figure 12. Garnet element distribution maps, BF-14P (migmatite zone): (a) Sc; (b) Cr; (c) Y; (d) P. The high-Sc/Cr/Y zone (white arrows) of this garnet is interpreted to have grown after moderate pressure (0.4 GPa < P < 0.5 GPa) dehydration melting of muscovite and during dehydration melting of biotite via the reaction biotite + sillimanite + plagioclase + quartz = garnet + K-feldspar + melt. Garnet contains xenotime in core and in low-Y rim (red arrow), but no xenotime is present in the high-Y zone produced during melting. Phosphorous zoning in garnet, within detection resolution of EMP, does not record the melting reaction. Width of image is approximately 8 mm. Ilm = ilmenite, Ap = apatite.

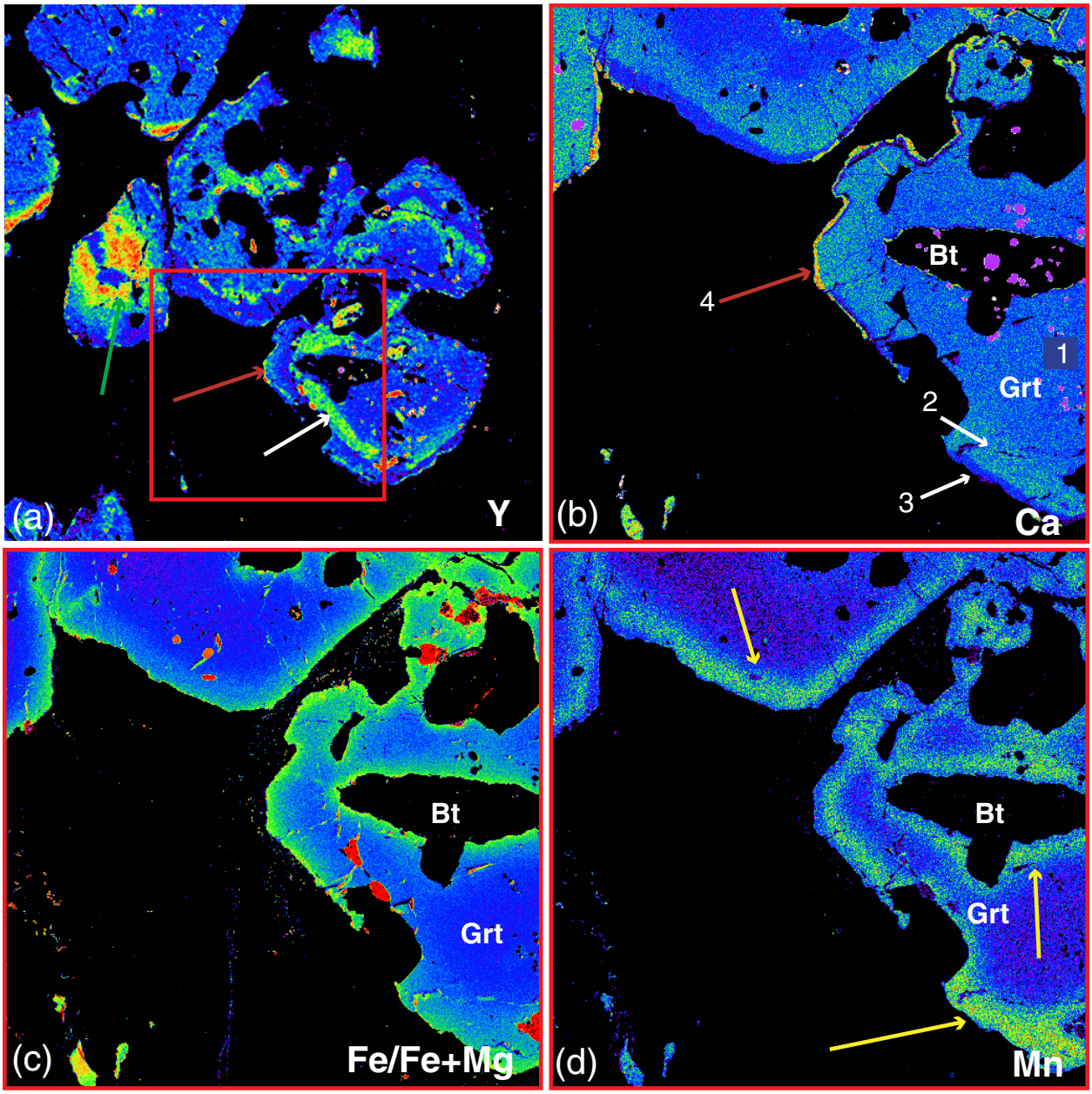

Figure 13. Comparison of Y and major-element distribution maps for migmatite zone sample K92-12 D: (a) Y; (b) Ca; (c) Fe/Fe+Mg; (d) Mn. Field of view in (a) is approximately 9 mm by 9 mm. Warm colors indicate higher concentrations of the mapped element. The high-Y zone in (a) (white arrow) has been interpreted by Kohn et al. (1997) as garnet that grew after dehydration melting of muscovite and during dehydration melting of biotite. Ca only weakly records the biotite melting event, and the biotite melting event is invisible to Mg, Mn, and Fe. A second high-Y zone on the extreme garnet rim (red arrows) corresponds to the extreme rim enrichment in Ca. The controlling factor in major-element distribution appears to be post-peak diffusive exchange between garnet and both matrix and included biotite, which is especially evident in the Mn distribution map (yellow arrows in (d)). Grt = garnet, Bt = biotite. See text for explanation of numbers 1-4 in (b).

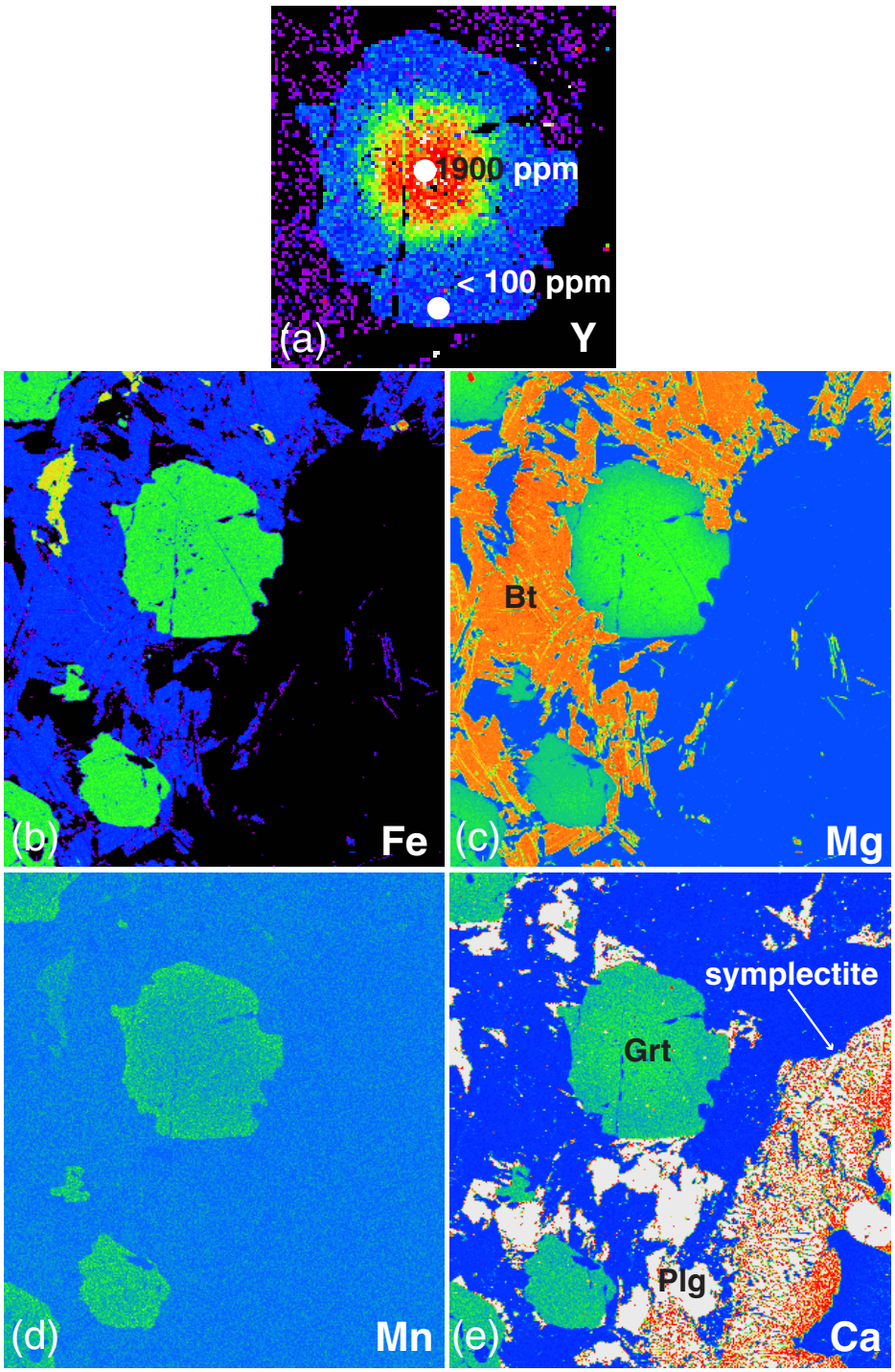

Figure 14. Comparison of yttrium and major-element distribution in garnet, sample LM-1A2 from the garnet-cordierite zone (peak conditions 700-730 ˚C, 0.2-0.4 GPa) of central New Hampshire. (a) Y. (b) Fe. (c) Mg. (d) Mn. (e) Ca. Garnet diameter approximately 1.2 mm. Symplectite in (e) = quartz + plagioclase symplectite. Major elements were homogenized near the metamorphic peak and modified by diffusion towards the rim during retrograde net transfer reactions. Strong Y zoning reflects growth of core at modest grade (T ≈ 550 ˚C) and little diffusional reequilibration of Y. Grt = garnet, Plg = plagioclase, Bt = biotite.

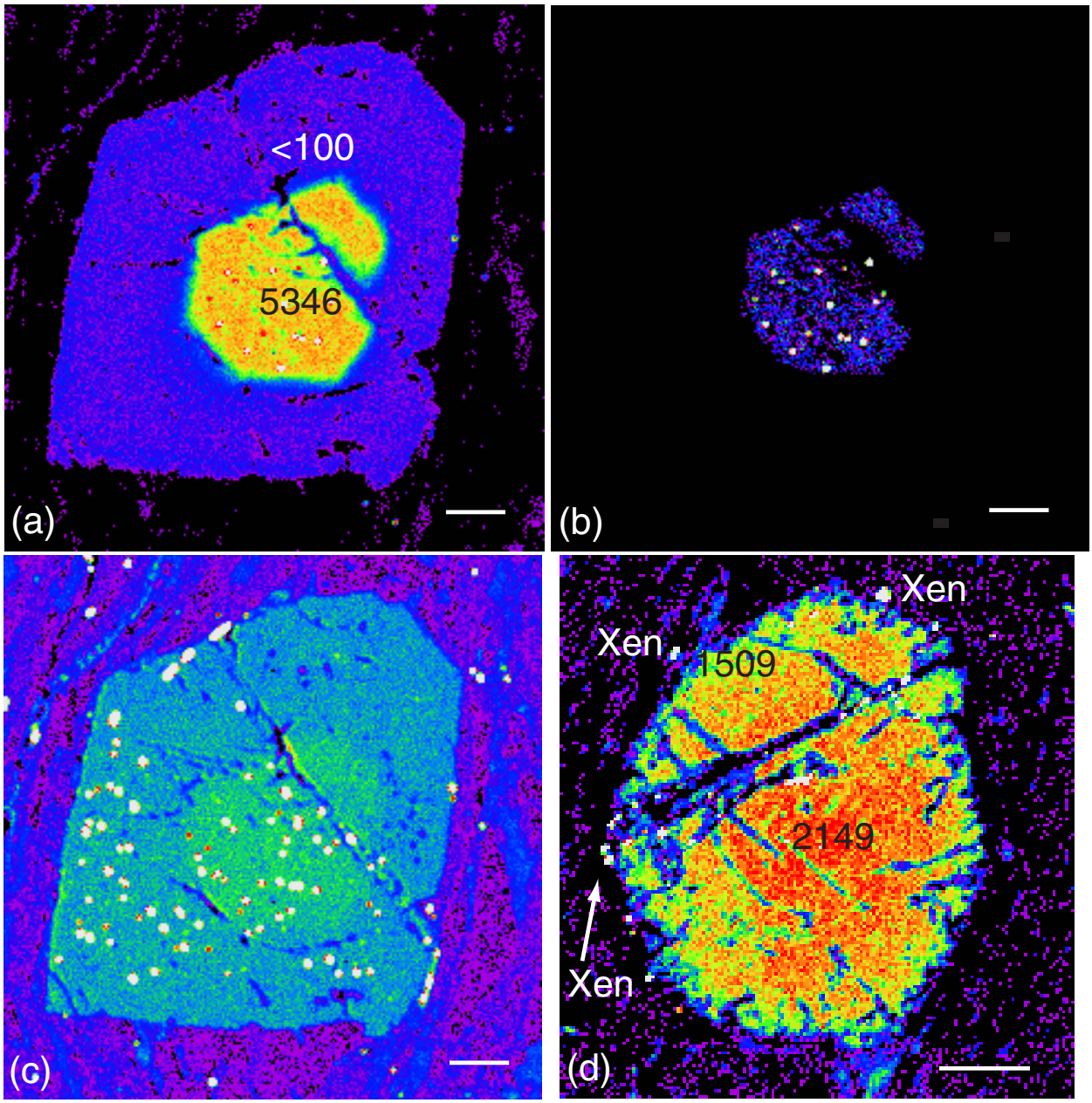

Figure 15. Garnet element distribution maps displaying correlation between the location of xenotime core inclusions and garnet yttrium and phosphorus distribution. (a) Sample BF-17A (staurolite zone) with high-yttrium core (5346 ppm Y) containing xenotime inclusions and low-yttrium outer region of garnet devoid of xenotime inclusions. (b) Y map from Fig. 15a scaled to display xenotime (white dots) restriction to high-Y garnet core. (c) Phosphorus distribution map of same garnet. Phosphates (white spots) occur throughout sample; apatite is present in garnet high-Y core, low-Y intermediate zone, and matrix. Monazite is present in the low-Y region of garnet and matrix, but not in the high-Y core. (d) Garnet Y map, sample 93-19A (garnet zone). Sample contains matrix xenotime and garnet that smoothly decreases in [Y] from core to rim. All scale bars = 100 µm. Grt = garnet, Bt = biotite, Ms = muscovite, Xen = xenotime.

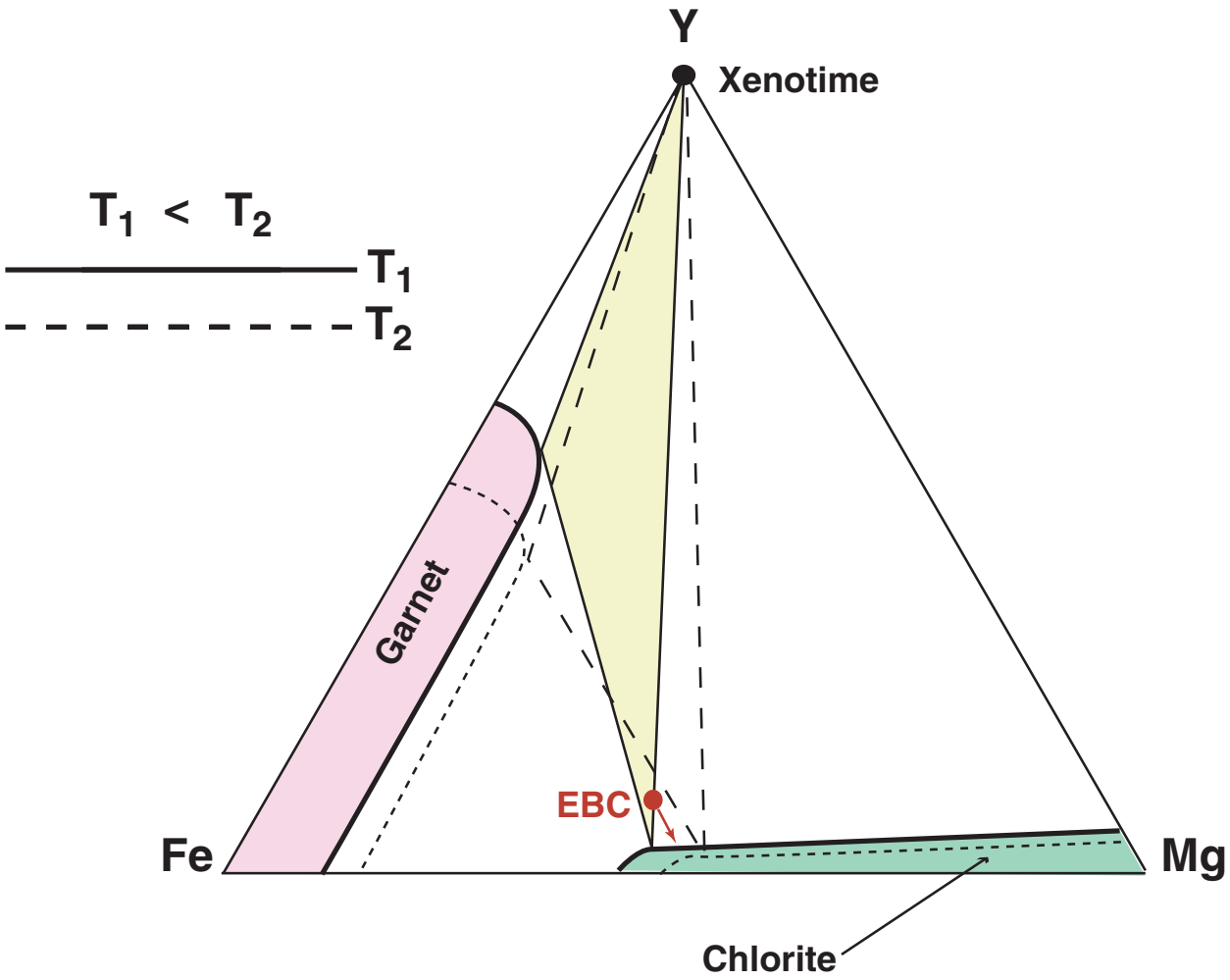

Figure 16. Qualitative, pseudo-ternary representation of the compositional relationships between garnet, chlorite, and xenotime at two different temperatures. Solid lines: phase relations at T_1. Dashed lines: three-phase relations at $T_2 > T_1$. Dotted lines: garnet and chlorite solid solution fields at T_2. Red circle indicates effective bulk composition (EBC). Red arrow shows trace of EBC with increasing T, assuming garnet growth fractionates Y, Fe, and Mg. At T_2, equilibrium Y content of garnet (and chlorite) has decreased relative to T_1, and garnet-chlorite Fe-Mg exchange sweeps the 3-phase garnet-chlorite-xenotime triangle towards more Mg-rich compositions, stranding the EBC in the 2-phase garnet-chlorite region. Y content of both garnet and chlorite exaggerated for clarity of presentation.

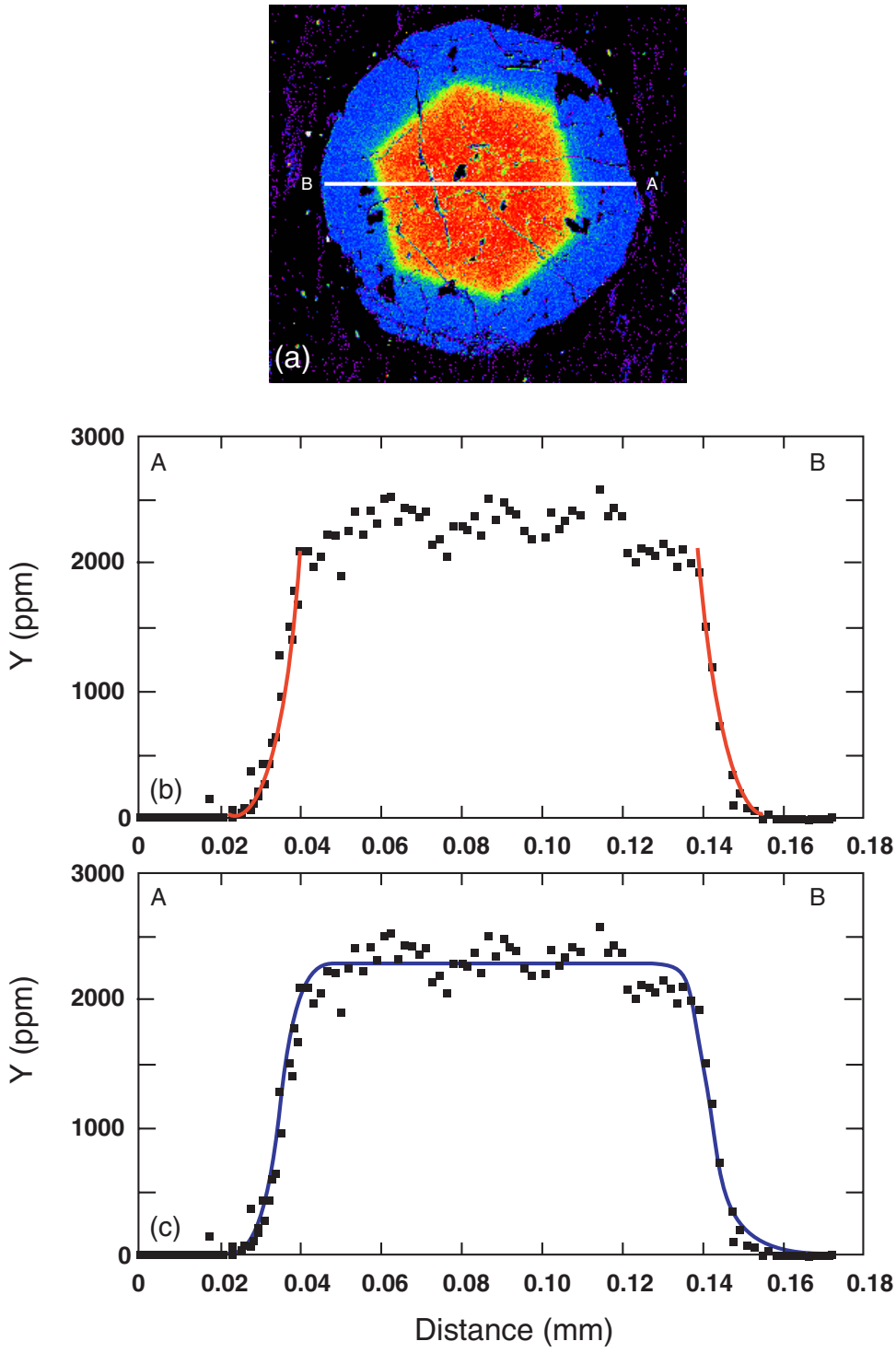

Figure 17. (a) X-ray map showing Y zoning in garnet and location of traverse in sample BF-58B (staurolite zone). (b) Rayleigh fractionation model of outer part of zoning profile. For this model, bulk distribution coefficient (garnet-rock) $\lambda = 200$, bulk-rock yttrium content $Y_0 = 10.5$ ppm, and garnet nucleation density = 125 cm^{-3} (garnet volume = 7.8%). (c) One-dimensional diffusion model to garnet Y zoning profile, sample BF-58B. Core modeled with homogeneous Y content of 2300 ppm. Zoning profile modeled with $D = 1.2 \times 10^{-20}$ $cm^2 sec^{-1}$, time = 25 Ma.

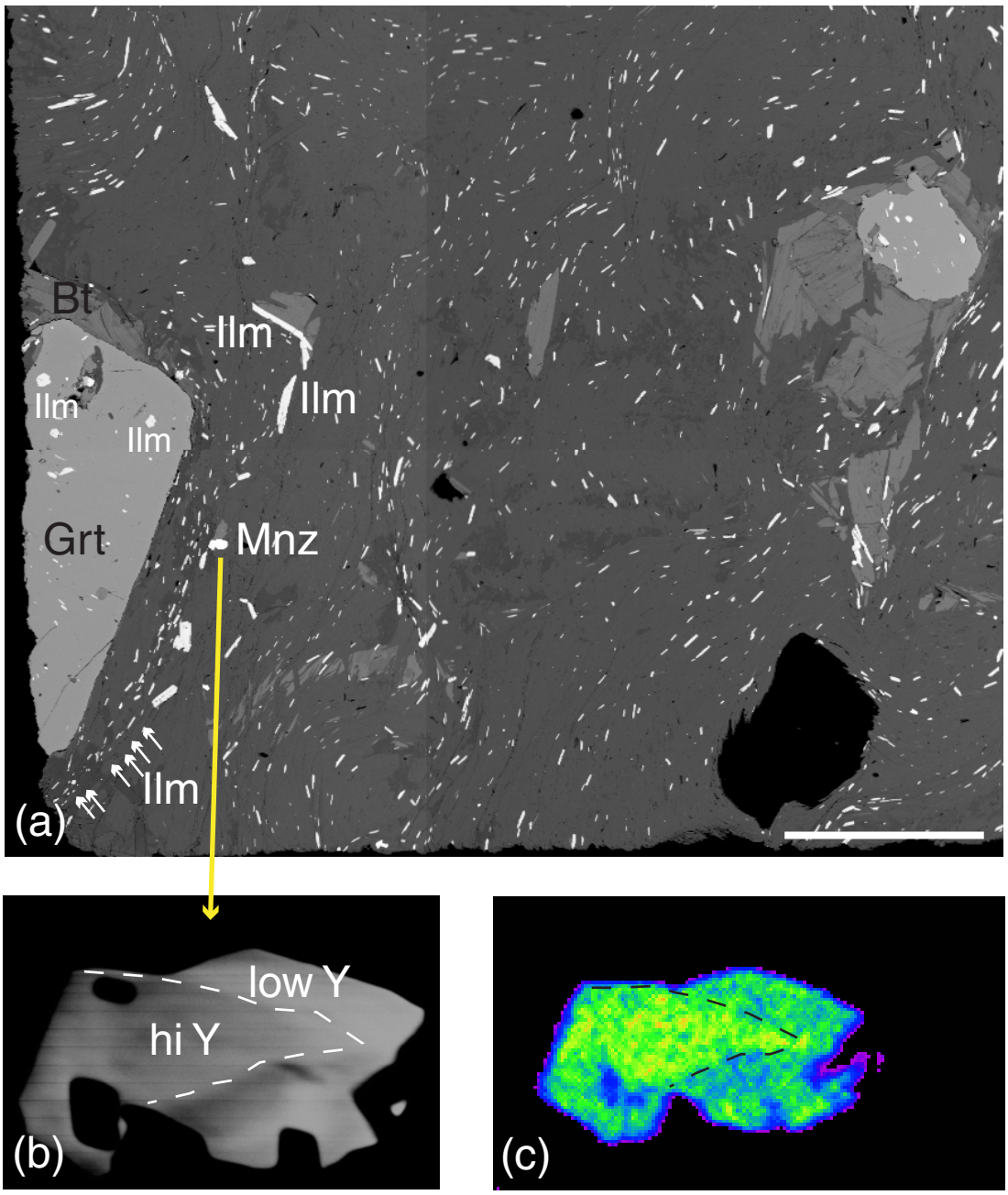

Figure 18. BEIs and X-ray image showing phosphates precipitated in zone of garnet resorption by reaction (2): garnet + chlorite + muscovite = staurolite + biotite + quartz + water. (a) Low-magnification BEI showing resorption zone outlined by Fe-Ti oxides and phosphates (bright grains). Ilmenite lineation shows that garnet resorption was evenly distributed (euhedral) around former garnet rim. Resorption zone is 300-500 µm wide. Arrow shows location of (b). (b) High magnification BEI showing zoned monazite at edge of garnet resorption zone. (c) Y X-ray map of monazite shown in (b). Y content of monazite increases in the direction of garnet rim and presumably the Y-enriched monazite was precipitated because of Y release during garnet resorption. Width of grain = 100 µm. Bt = biotite, Grt = garnet, Ilm = ilmenite, Mnz = monazite.

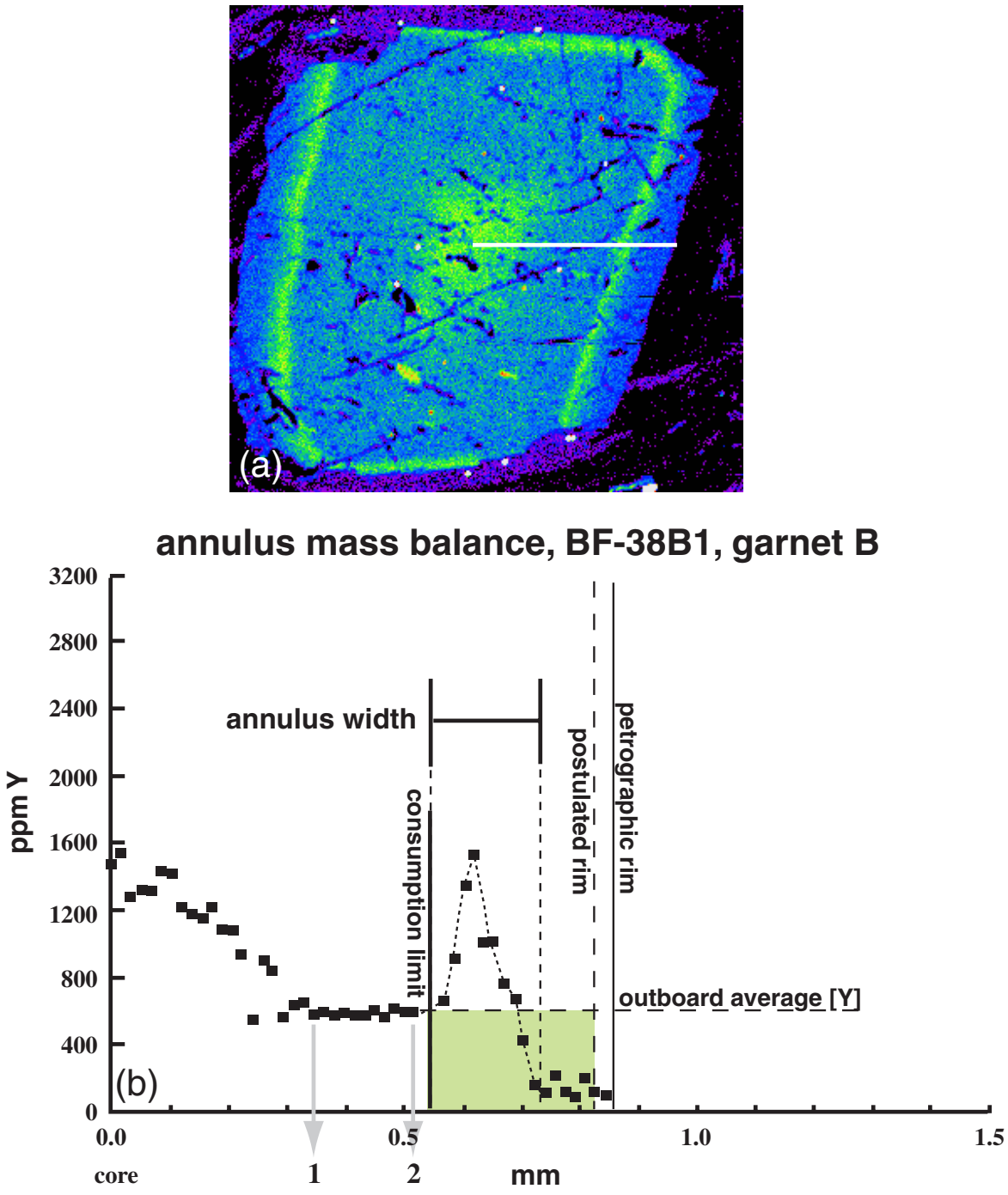

Figure 19. Annulus mass-balance, sample BF-38B1, garnet B. (a) Garnet Y distribution map. Line on Y distribution map indicates position of traverse. (b) Annulus mass balance. Postulated pre-consumption outboard average concentration of Y is taken as the average of point analyses from point 1 to point 2 (point 2 = maximum coreward extent of garnet consumption). Area under annulus (indicated by short dotted line connecting traverse points) is equal to area in green (adjusted for assumed spherical geometry). Assumption of equally distributed radial consumption places postulated pre-staurolite garnet rim approximately 0.03 mm inside of the petrographic rim.

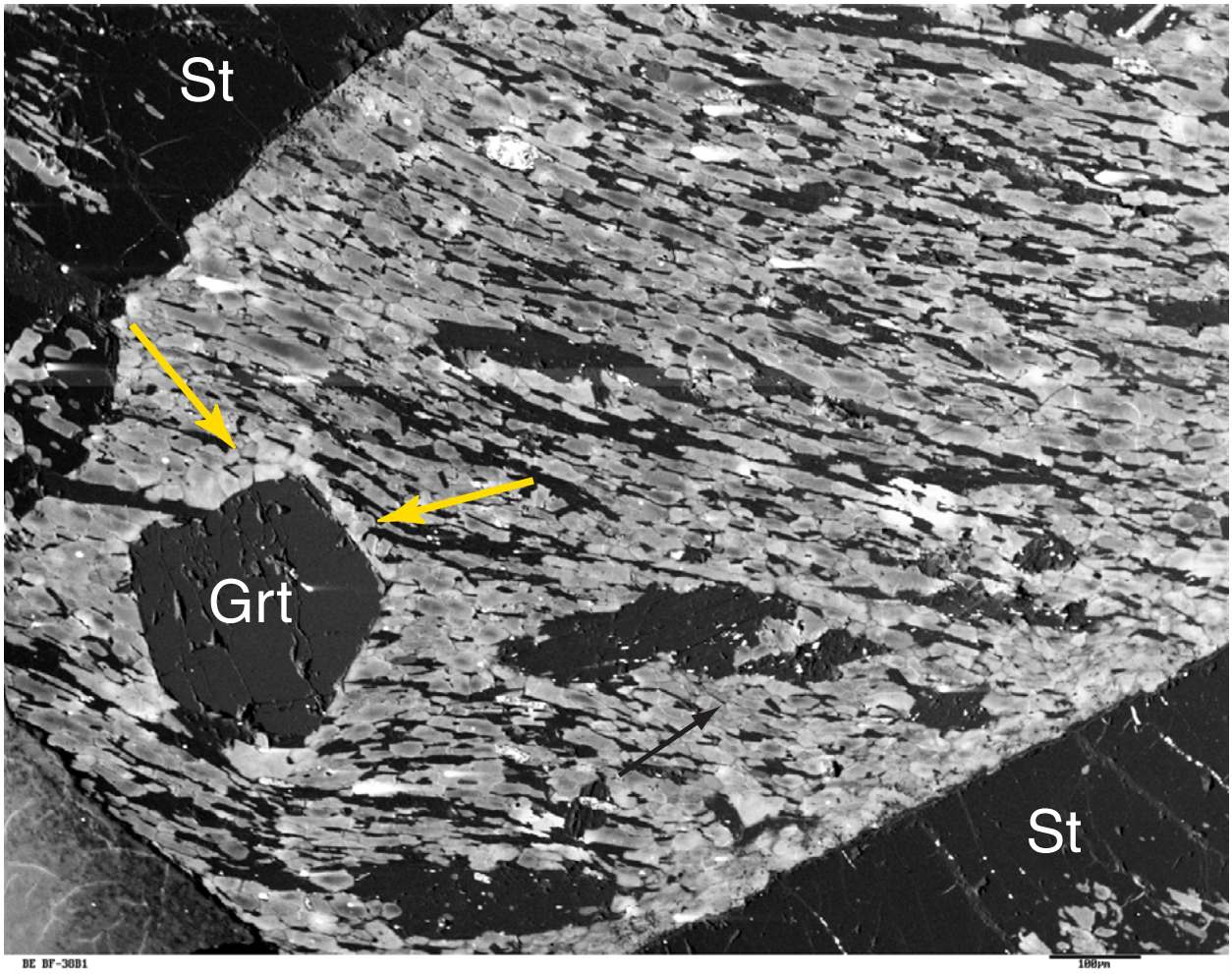

Figure 20. Cathode luminescence image of staurolite zone sample BF-38B1. Yellow arrows point to quartz surrounding garnet that displays brighter luminescence than quartz farther from garnet (black arrow). Brighter quartz is interpreted to have formed during garnet resorption by reaction (2): garnet + chlorite + muscovite = staurolite + biotite + quartz + water. Field of view is 1.3 mm. Grt = garnet, St = staurolite.

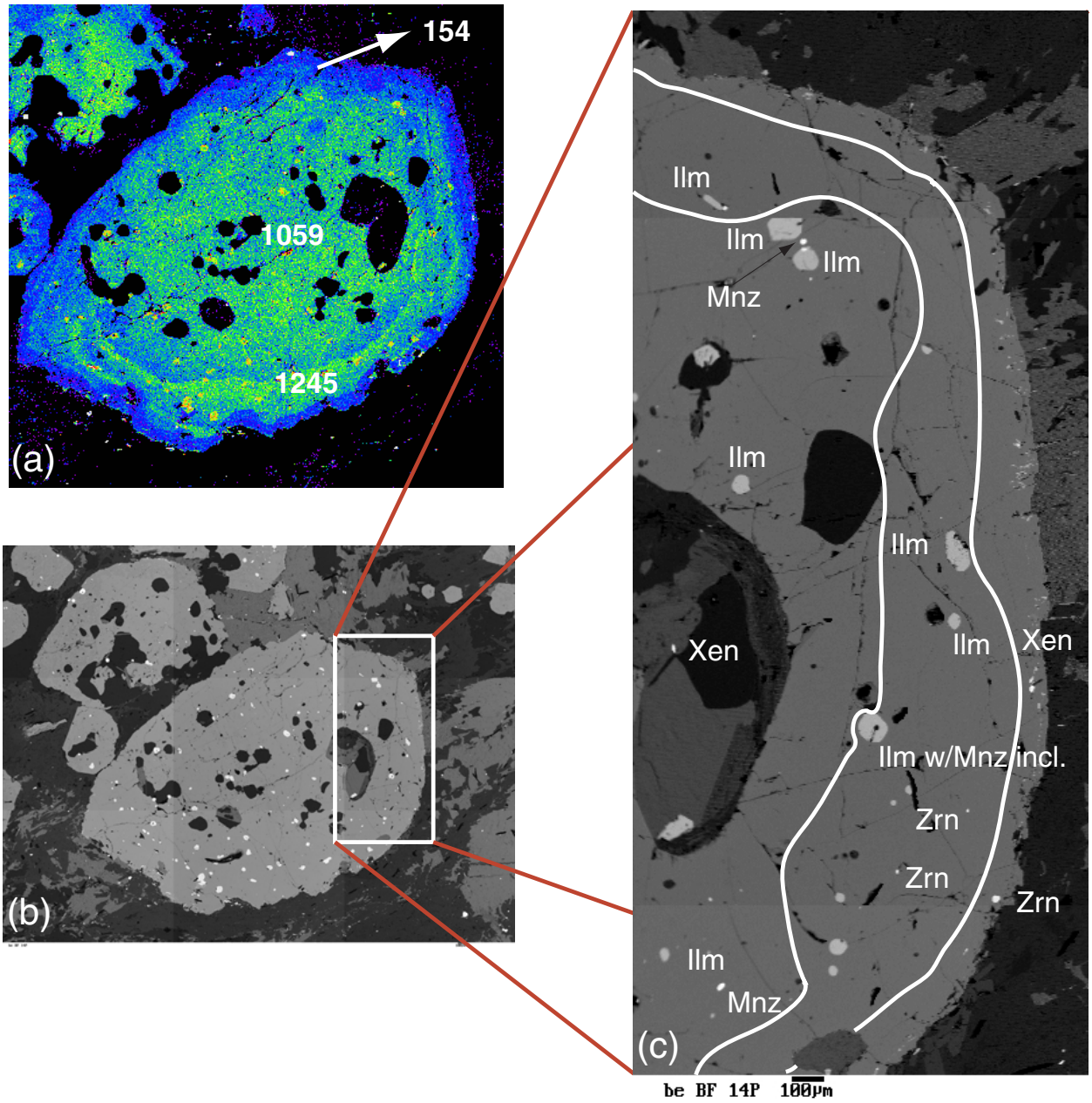

Figure 21. Y distribution map (a) and BEI (b) of garnet in anatectic sample BF-14P, with enlargement (c) of region of garnet interpreted to have grown after muscovite dehydration melting and during biotite dehydration melting (area enclosed by white lines). Phosphates monazite and xenotime are found in the garnet core, but no phosphates are found in the high (Cr, Y) region (between white lines in c), with the exception of a single monazite grain included in ilmenite. Xenotime occurs as inclusions in garnet outboard of the high Y zone. Ilm = ilmenite, Mnz = monazite, Xen = xenotime, Zrn = zircon. Width of images (a) and (b) approximately 8 mm. Scale bar in (c) = 100 µm. Numbers = Y concentrations in ppm.